

Dependence of Ice Crystal Size Distributions in High Ice Water Content Conditions on Environmental Conditions: Results from the HAIC-HIWC Cayenne Campaign

YACHAO HU,^{a,b} GREG M. MCFARQUHAR,^{b,c} PETER BRECHNER,^{b,c} WEI WU,^b YONGJIE HUANG,^{c,d} ALEXEI KOROLEV,^e ALAIN PROTAT,^f CUONG NGUYEN,^g MENGISTU WOLDE,^g ALFONS SCHWARZENBOECK,^h ROBERT M. RAUBER,ⁱ AND HONGQING WANG^a

^a Department of Atmospheric and Oceanic Sciences, School of Physics, Peking University, Beijing, China

^b Cooperative Institute for Severe and High Impact Weather Research and Operations, University of Oklahoma, Norman, Oklahoma

^c School of Meteorology, University of Oklahoma, Norman, Oklahoma

^d Center for Analysis and Prediction of Storms, University of Oklahoma, Norman, Oklahoma

^e Environment and Climate Change Canada, Toronto, Ontario, Canada

^f Australian Bureau of Meteorology, Melbourne, Victoria, Australia

^g National Research Council Canada, Ottawa, Ontario, Canada

^h Laboratoire de Météorologie Physique, UCA, CNRS, Aubière, France

ⁱ Department of Atmospheric Sciences, University of Illinois at Urbana-Champaign, Urbana, Illinois

(Manuscript received 18 January 2022, in final form 14 June 2022)

ABSTRACT: A new method that automatically determines the modality of an observed particle size distribution (PSD) and the representation of each mode as a gamma function was used to characterize data obtained during the High Altitude Ice Crystals and High Ice Water Content (HAIC-HIWC) project based out of Cayenne, French Guiana, in 2015. PSDs measured by a 2D stereo probe and a precipitation imaging probe for particles with maximum dimension (D_{\max}) $> 55 \mu\text{m}$ were used to show how the gamma parameters varied with environmental conditions, including temperature (T) and convective properties such as cloud type, mesoscale convective system (MCS) age, distance away from the nearest convective peak, and underlying surface characteristics. Four kinds of modality PSDs were observed: unimodal PSDs and three types of multimodal PSDs (Bimodal1 with breakpoints $100 \pm 20 \mu\text{m}$ between modes, Bimodal2 with breakpoints $1000 \pm 300 \mu\text{m}$, and Trimodal PSDs with two breakpoints). The T and ice water content (IWC) are the most important factors influencing the modality of PSDs, with the frequency of multimodal PSDs increasing with increasing T and IWC. An ellipsoid of equally plausible solutions in $(N_o-\lambda-\mu)$ phase space is defined for each mode of the observed PSDs for different environmental conditions. The percentage overlap between ellipsoids was used to quantify the differences between overlapping ellipsoids for varying conditions. The volumes of the ellipsoid decrease with increasing IWC for most cases, and $(N_o-\lambda-\mu)$ vary with environmental conditions related to distribution of IWC. HIWC regions are dominated by small irregular ice crystals and columns. The parameters $(N_o-\lambda-\mu)$ in each mode exhibit mutual dependence.

KEYWORDS: South America; Tropics; Mesoscale systems; Cirrus clouds; Cloud microphysics; Ice crystals

1. Introduction

Cirrus covers 20%–30% of Earth (Heymsfield and McFarquhar 2002; Wylie et al. 2005), and affects the vertical profile of radiative heating (e.g., Ackerman et al. 1988). Anvil cirrus shields produced when convective ice detains into the upper troposphere can significantly impact the atmosphere's radiation budget (e.g., Machado and Rossow 1993; Fu et al. 1995; Zender and Kiehl 1997; Del Genio and Kovari 2002; Stephens 2005). The size, shape, and concentration of ice particles in cirrus have a large impact on cloud radiative forcing, and hence determine cloud feedbacks that modify estimates of global climate change (Ackerman et al. 1988; Mitchell et al. 2008; Sanderson et al. 2008; Lawson et al. 2010). In addition, ice microphysical properties are of particular importance due to the strong sensitivity of simulated deep convective systems to parameterizations of microphysical process rates (Chen and Cotton 1988; McCumber et al. 1991; Gilmore et al. 2004;

Milbrandt and Yau 2005; McFarquhar et al. 2006; Morrison and Grabowski 2008; Huang et al. 2020) that depend on the habits and size distributions of ice crystals.

The number distribution function [$N(D)$] of ice crystals determines many microphysical properties (e.g., ice water content IWC, total number concentration N_t , mass-weighted terminal velocity v_m , effective radius R_e , bulk extinction β , and single scattering properties), parameterizations of which are important for the Earth system models (e.g., Stephens 2005; Jakob and Klein 1999; Sanderson et al. 2008; Jackson et al. 2015) and weather models (e.g., Morrison et al. 2009; Bryan and Morrison 2012; Stanford et al. 2019) because they control distributions of latent heating and cooling, condensate loading and radiant fluxes (Schlimme et al. 2005) that are directly coupled with model dynamics (Morrison et al. 2015). Mass-weighted terminal velocity determined by particle size distributions (PSDs) controls the cloud coverage and lifetime simulated by climate models (Sanderson et al. 2008), and impacts spatial distributions of latent heating by affecting microphysical process rates (i.e., riming aggregation, melting, evaporation, etc.). Further, the accuracy of cirrus remote

Corresponding author: Greg McFarquhar, mcfarq@ou.edu

sensing retrievals depends on accurate representations of PSDs (Wolf et al. 2019). The effective diameter (D_e) depends on PSDs and is commonly used to parameterize single scattering properties needed for calculation of shortwave radiative transfer (e.g., Fu 1996; McFarquhar and Heymsfield 1998; Mitchell 2002). The radar reflectivity is a higher-order moment of PSDs in the Rayleigh scattering regime (Smith 1984). Thus, correct interpretation of ice crystal PSDs is critically needed for development and evaluation of model parameterization schemes and remote sensing retrievals (Gu et al. 2011).

Many microphysical parameterization schemes, such as the Milbrandt two-moment scheme (Milbrandt and Yau 2005), the Thompson scheme (Thompson et al. 2008), the State University of New York at Stony Brook scheme by Yanluan Lin (SBU-YLIN; Lin and Colle 2011), and the predicted particle properties (P3) scheme (Morrison and Milbrandt 2015) make assumptions about the number and type of categories of the hydrometeors present and the shape of the PSDs in each category. A plethora of studies found considerable sensitivity of high-resolution numerical weather prediction forecasts to the selection of the microphysics schemes and the use of parameters in such schemes (e.g., Wang 2002; McFarquhar et al. 2006; 2012; Zhu and Zhang 2006; Li and Pu 2008; Van Weverberg et al. 2011; Clark et al. 2012; Huang et al. 2020).

PSDs have been fit using exponential or gamma functions in many parameterization schemes (e.g., Walko et al. 1995; Meyers et al. 1997; Straka and Mansell 2005; Milbrandt and Yau 2005). The gamma function used to represent the number distribution function $N(D_{\max})$ is typically represented by

$$N(D_{\max}) = N_o D_{\max}^{\mu} e^{-\lambda D_{\max}}, \quad (1)$$

where N_o is the intercept, D_{\max} is the maximum crystal dimension, λ is the slope, and μ is the dispersion parameter (e.g., Gilmore et al. 2004; Straka and Mansell 2005; Milbrandt and Yau 2005; Moisseev and Chandrasekar 2007; Wolf et al. 2019; Chen et al. 2020). However, the units of N_o vary with μ in Eq. (1). Thus, the gamma function can alternately be written as

$$N(D_{\max}) = N_o \left(\frac{D_{\max}}{D_o} \right)^{\mu} e^{-\lambda D_{\max}}, \quad (2)$$

where $D_o = 1 \text{ cm}$ is frequently assumed so that N_o has identical units to $N(D_{\max})$ ($\text{cm}^{-3} \mu\text{m}^{-1}$ or m^{-4} ; McFarquhar et al. 2015; Mascio et al. 2020).

Knowledge about the dependence of N_o , λ , and μ on environmental conditions is important, because such parameters affect the simulation of cloud properties (e.g., McCumber et al. 1991; McFarquhar et al. 2006). Many in situ observations have been used to fit the measured PSDs (e.g., Gunn and Marshall 1958; Wong et al. 1988; Heymsfield and McFarquhar 2002; Heymsfield et al. 2009; McFarquhar and Black 2004; McFarquhar et al. 2007) by different techniques to minimize the difference between the observed PSDs and fitted $N(D)$. For example, the least squares method (e.g., McFarquhar and Heymsfield 1997), the method of moments (e.g., Field et al. 2005; Smith and Kliche 2005; Smith et al. 2009; Tian et al.

2010; Handwerker and Straub 2011), and the maximum-likelihood approach (e.g., Haddad et al. 1996) have all been used. Sometimes uncertainty has been taken into account when estimating the fit parameters for observed PSDs to improve the fitting techniques (e.g., Wong and Chidambaram 1985; Chandrasekar and Bringi 1987; Moisseev and Chandrasekar 2007; Smith et al. 2009; Handwerker and Straub 2011). McFarquhar et al. (2015) developed an Incomplete Gamma Fitting (IGF) Technique that uses statistical uncertainty and variability in microphysical properties within a family of distributions to represent the fit parameters as an ellipsoid of equally realizable solutions in (N_o, λ, μ) phase space. The results showed that N_o , λ , and μ exhibited some mutual dependence, which must be accounted for when applying the results of the fits.

This technique has been used to study how the ellipsoids describing gamma distributions vary with environmental conditions (e.g., Mascio et al. 2020) and complement other studies showing how the most likely fit parameters vary with environmental conditions (e.g., Thompson et al. 2008; Tian et al. 2010). However, these studies did not consider the multimodal properties of PSDs even though previous studies showed two peaks in measured PSDs (e.g., Varley 1978; Mitchell 1996; McFarquhar and Heymsfield 1997; Jensen et al. 2009; Zhao et al. 2010; Lawson et al. 2010). Breakpoints between these peaks or between the two modes in the PSDs sometimes occurred at a size near the cutoff between two instruments used to measure the PSDs (e.g., McFarquhar and Heymsfield 1997; Zhao et al. 2010), but also frequently occurred at sizes not near the cutoff between instruments (e.g., Jackson et al. 2015). Further, peaks and breakpoints were also found in PSDs measured by only one probe (e.g., Mitchell 1996; Jensen et al. 2009). Attempts to parameterize multimodal size distributions include those by Welch et al. (1980) who used two modified gamma distribution and Jackson et al. (2015) who extended the McFarquhar et al. (2015) IGF technique to allow for a bimodal gamma distribution function. Although these studies improved the understanding on the distribution of ice crystals, sufficient data were not yet available to characterize the PSDs from tropical zones and high IWC regions.

The High Altitude Ice Crystals (HAIC; Dezitter et al. 2013) and High Ice Water Content (HIWC; Strapp et al. 2016a) projects collected airborne in situ and remote sensing data from large oceanic convective clouds, with the primary objective of collecting a dataset of high IWC measurements for assessment of a new aircraft certification envelope for the ice crystal environment (Strapp et al. 2021). Campaigns were performed using the French Falcon-20 out of Darwin, Australia, in 2014 (Leroy et al. 2017) and Cayenne, French Guiana, in 2015 (Dezitter et al. 2013; Strapp et al. 2016a), whereas the HIWC-RADAR flight campaign out of Florida in 2015 (Yost et al. 2018, Ratavsky et al. 2019) used the NASA DC-8. The HAIC-HIWC data provide a wealth of in-cloud microphysical measurements that have been used to investigate HIWC regions (e.g., Protat et al. 2016; Wolde et al. 2016; Fontaine et al. 2017; Leroy et al. 2016a,b, 2017; Qu et al. 2018; Yost et al. 2018; Huang et al. 2021). For example, a companion study

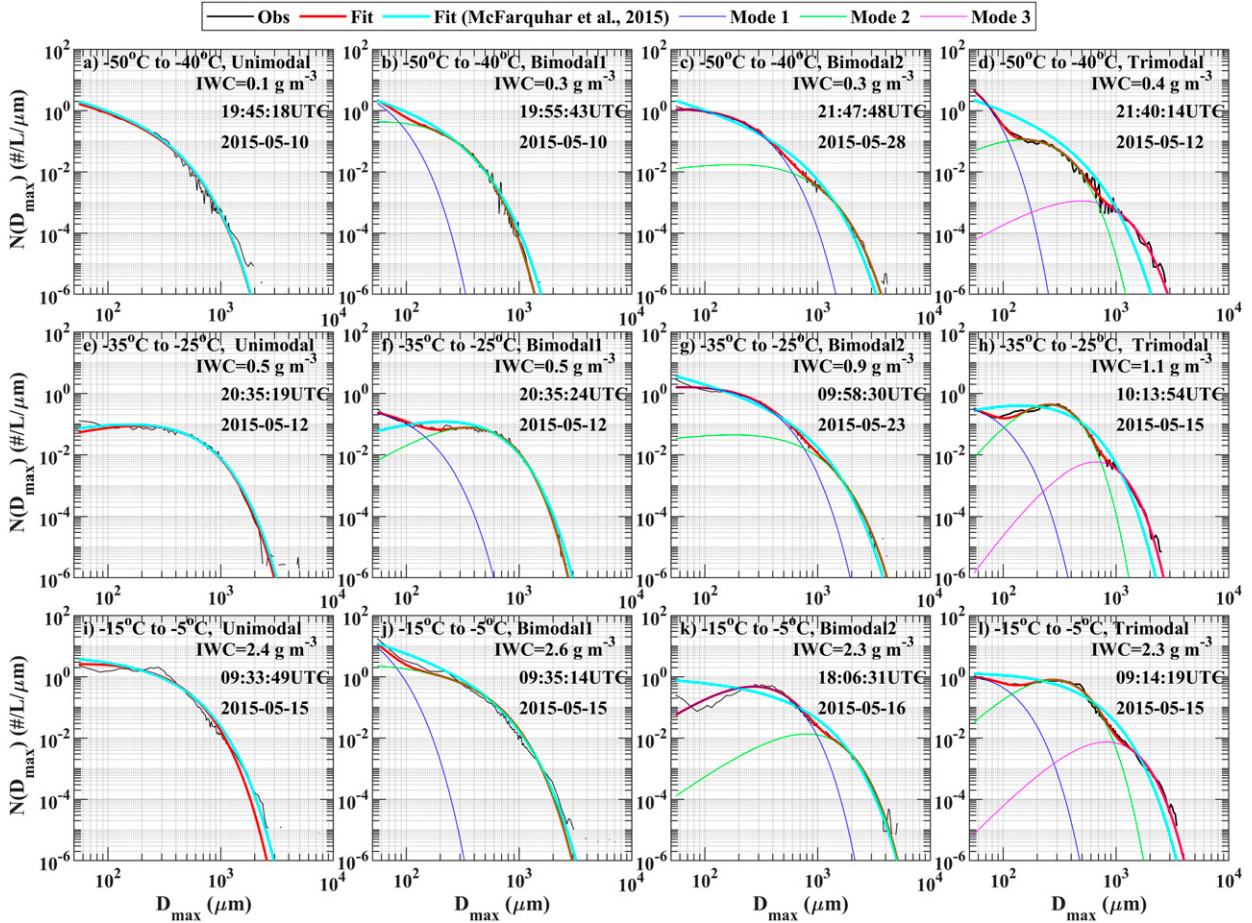


FIG. 1. Example of different modality PSDs and fits to those PSDs as a function of T using data obtained during the HAIC-HIWC Cayenne campaign. (a) Unimodal, (b) Bimodal1, (c) Bimodal2, and (d) Trimodal PSDs at $-50^{\circ} \leq T \leq -40^{\circ}\text{C}$. (e)–(h) As in Figs. 1a–d, but for $-35^{\circ} \leq T \leq -25^{\circ}\text{C}$. (i)–(l) As in Figs. 1a–d, but for $-15^{\circ} \leq T \leq -5^{\circ}\text{C}$. Black lines indicate observed PSDs; red lines fits to observed PSD using method of Brechner (2021) that automatically determines number of modes in PSDs; cyan lines represent fit assuming unimodal distribution using the algorithm of McFarquhar et al. (2015); and blue, green, and pink lines indicate fits to first, second, and third mode of PSD, respectively.

(Hu et al. 2021) investigated the dependence of IWC and median mass diameter (MMD) on environmental conditions (e.g., temperature, vertical velocity, underlying surface characteristics defined as whether the surface was land, ocean, or coastline, mesoscale convective system (MCS) age, the distance away from the convective core and the local strength of convection) for data obtained from the Cayenne field campaign.

Brechner (2021) developed a new method that automatically identifies the existence of up to three peaks in PSDs, integrating each mode over all crystal sizes rather than having an artificial breakpoint between modes for PSDs as done by Jackson et al. (2015). Brechner's (2021) method was used to investigate the nature of PSDs measured during the first phase of the HAIC-HIWC field campaign collected in Darwin, Australia, in 2014. The analysis of data collected during the second HAIC-HIWC campaign field conducted from 9 to 29 May 2015 out of Cayenne, French Guiana, presented in Hu et al. (2021) is extended here to quantitatively describe the dependence of PSDs on IWC and environmental conditions.

The remainder of this paper is organized as follows. Section 2 describes the HAIC-HIWC dataset and methodology used to process the data. Section 3 presents a case study on the nature of different modality PSDs. Investigations of how statistical distributions of PSDs parameters vary with environmental conditions are shown in section 4. Section 5 summarizes the significance of this study and offers directions for future research.

2. Data and methodology

a. Overview of campaign

The second HAIC-HIWC flight campaign based out of Cayenne (French Guiana) 9–29 May 2015 collected in situ and remotely sensed data of oceanic convective clouds to characterize and improve the understanding of the high-altitude and high-concentration ice crystal environment. A total of 17 French Falcon-20 flights and 10 Canadian National Research Council (NRC) Convair-580 flights are used here.

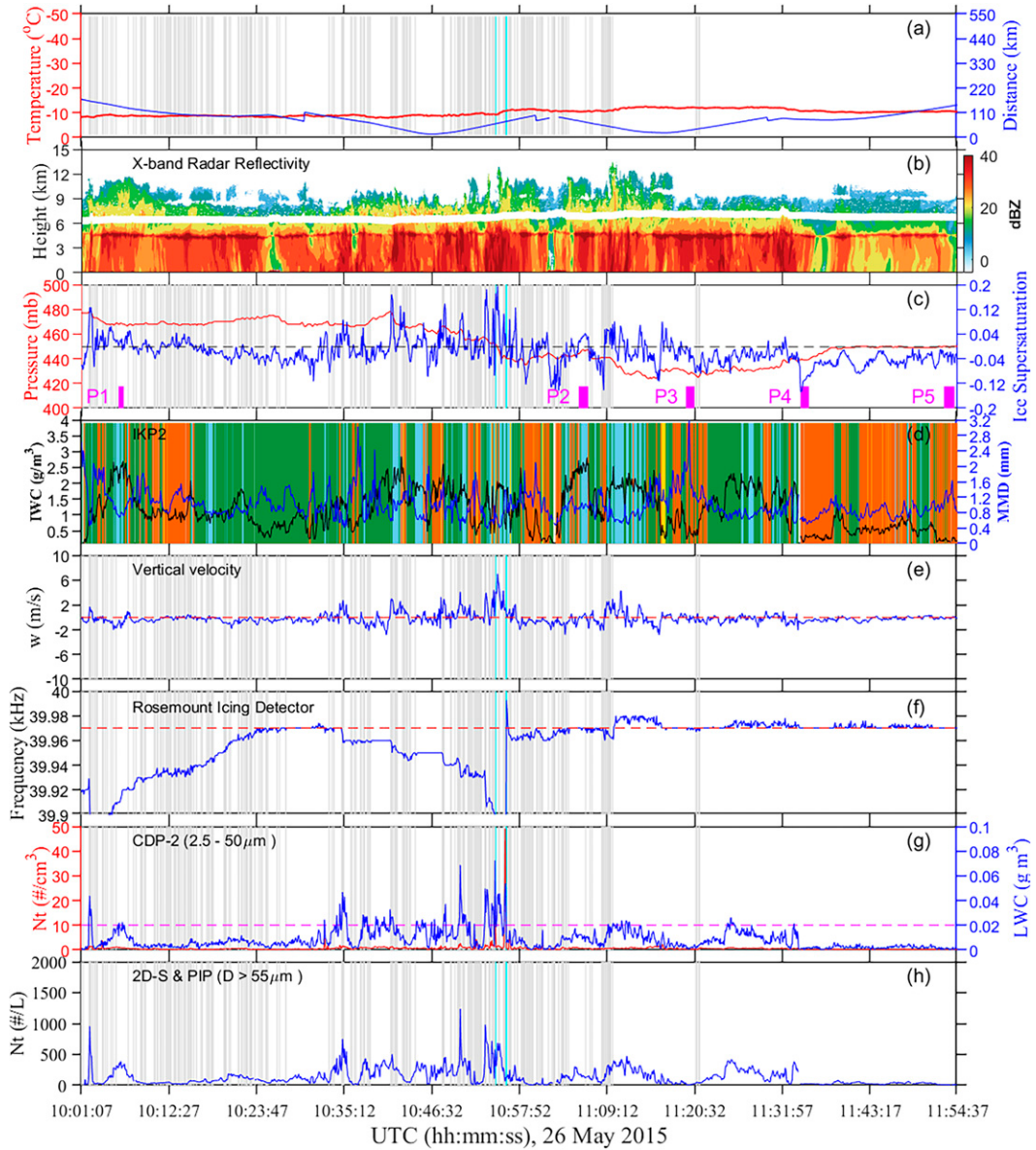


FIG. 2. Time series of (a) temperature at flight altitude (red line), distance away from convective core (L , blue line, times when aircraft out of MCS not shown); (b) X-band radar reflectivity from X- and W-band polarization radar mounted on Convair-580; (c) atmosphere pressure (red line) and ice supersaturation (blue line), with magenta rectangles P1–P5 representing five periods with their width along x axis denoting length of time period; (d) IWC from IKP2 (black line) and MMD (blue line), with shaded orange boxes representing locations of Unimodal PSDs, sky-blue boxes representing locations of Trimodal PSDs, yellow boxes representing locations of Bimodal1, and green boxes representing locations of Bimodal2 PSDs; (e) vertical velocity (w) measured by an Aventech Aircraft Integrated Meteorological Measurements System (AIMMS-20); (f) Rosemount icing detector frequency (blue line) with a threshold of 39.97 kHz indicating presence of supercooled liquid water (red line); (g) N_t (red line) and LWC (blue line) derived by integrating $N(D_{\max})$ measured by CDP for $2.5 < D_{\max} < 50 \mu\text{m}$, red line shows threshold of 10 cm^{-3} for N_t used to identify periods of liquid water; and (g) N_t from composite 2D-S ($D_{\max} > 55 \mu\text{m}$) and PIP size distribution for 1001:07–1154:37 UTC 26 May 2015 Convair-580 flight leg. Shaded gray boxes represent locations of Rosemount icing detector frequency less than 39.97 kHz, and shaded cyan boxes indicated N_t measured by CDP-2 larger than 10 cm^{-3} .

The Convair-580 did almost all of its sampling at levels corresponding to T of approximately -10°C due to its limited ceiling. The French Falcon-20, equipped with in situ cloud probes, conducted 17 flights in oceanic, coastal, and continental

MCSs at varying levels centered at temperatures of mostly -10° , -30° , and -45°C (Strapp et al. 2016a). The temperature refers to the location where the ice particles were measured, but this may not necessarily be the level where they grew.

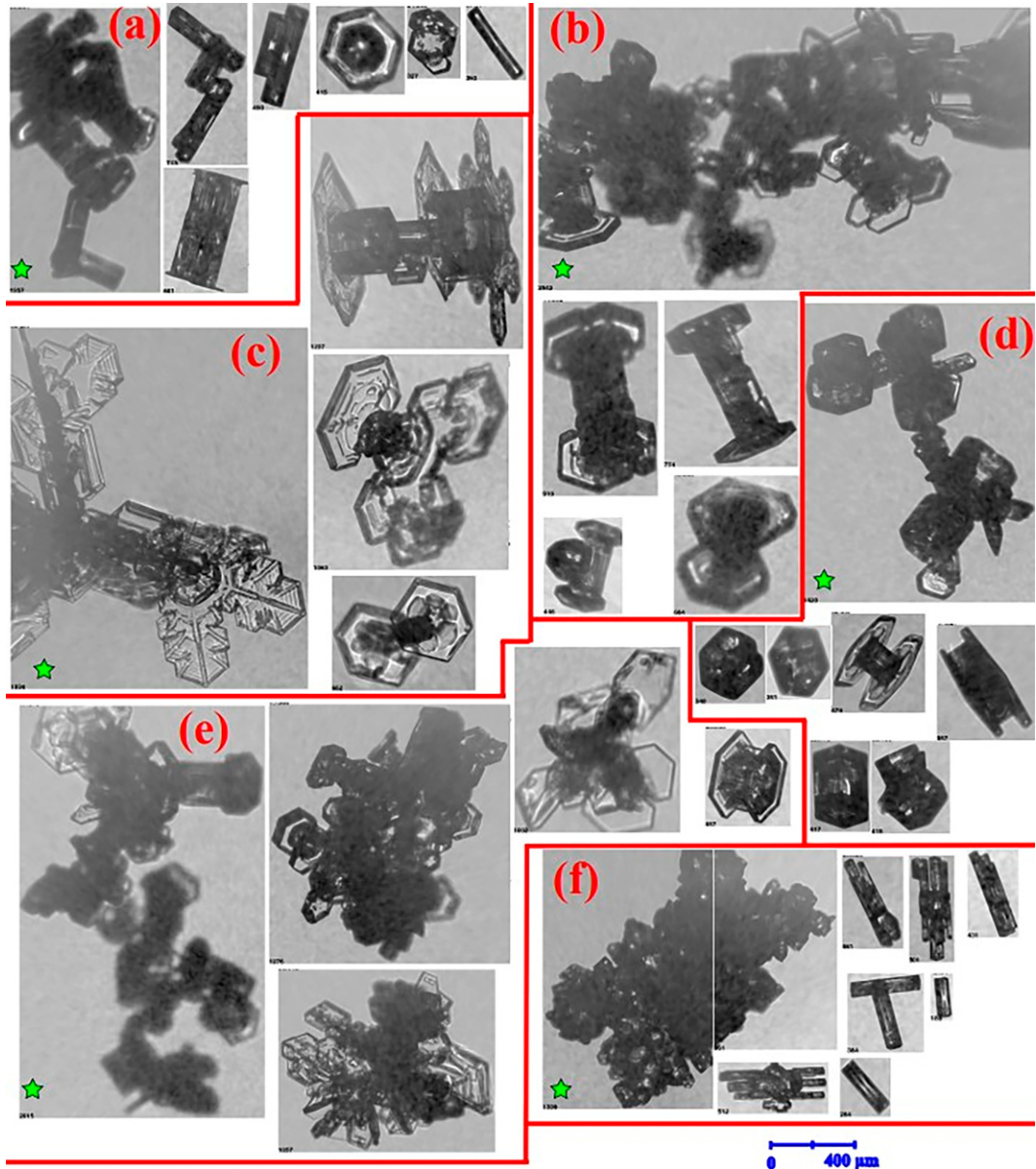


FIG. 3. Examples of representative ice crystals measured by SPEC CPI at (a) 1005:57–1006:37, (b) 1105:32–1106:47, (c) 1119:27–1120:32, (d) 1134:17–1135:22, and (e) 1152:52–1154:12 UTC 26 May 2015 corresponding to periods P1–P5 in Fig. 2c. (f) Typical ice crystals measured by SPEC CPI 1608:27–1609:27 UTC 26 May 2015. Ice crystal marked by green pentagram of each subgraph means the largest particle of that whole period.

Hu et al. (2021) discussed the flights conducted, the probes used and the procedures by which data were processed. Thus, only a brief summary of the most salient aspects is offered here.

b. In situ probes

Hu et al. (2021) summarized the cloud microphysics probes installed on the Falcon-20. These probes include a Stratton Park Engineering (SPEC 2011) two-dimension stereo probe [2D-S; nominally sizing diameter (D) between 10 and 1280 μm], a Droplet Measurement Technologies (DMT 2009) precipitation image probe (PIP; 100–6400 μm), a DMT Cloud Droplet Probe

(CDP-2; 2–49 μm), an isokinetic evaporator probe (IKP2; $\sim 0.1\text{--}10 \text{ g m}^{-3}$ at 200 m s^{-1}) for the primary measurement of bulk total water content TWC (Strapp et al. 2016b), a Science Engineering Associates (SEA) Robust hot wire TWC probe, a Rosemount Icing Detector, and a multibeam 95 GHz Doppler cloud radar (RADar SysTem Airborne, RASTA). The Convair-580 was equipped with polarization radar (X and W-band, 9.41 GHz and 94.05 GHz) and a suite of in situ cloud particle probes, including a 2D-S, a DMT PIP, a DMT CDP-2, an IKP2, where the parameters of these probes are the same as those mounted on Falcon-20. In addition, a Particle

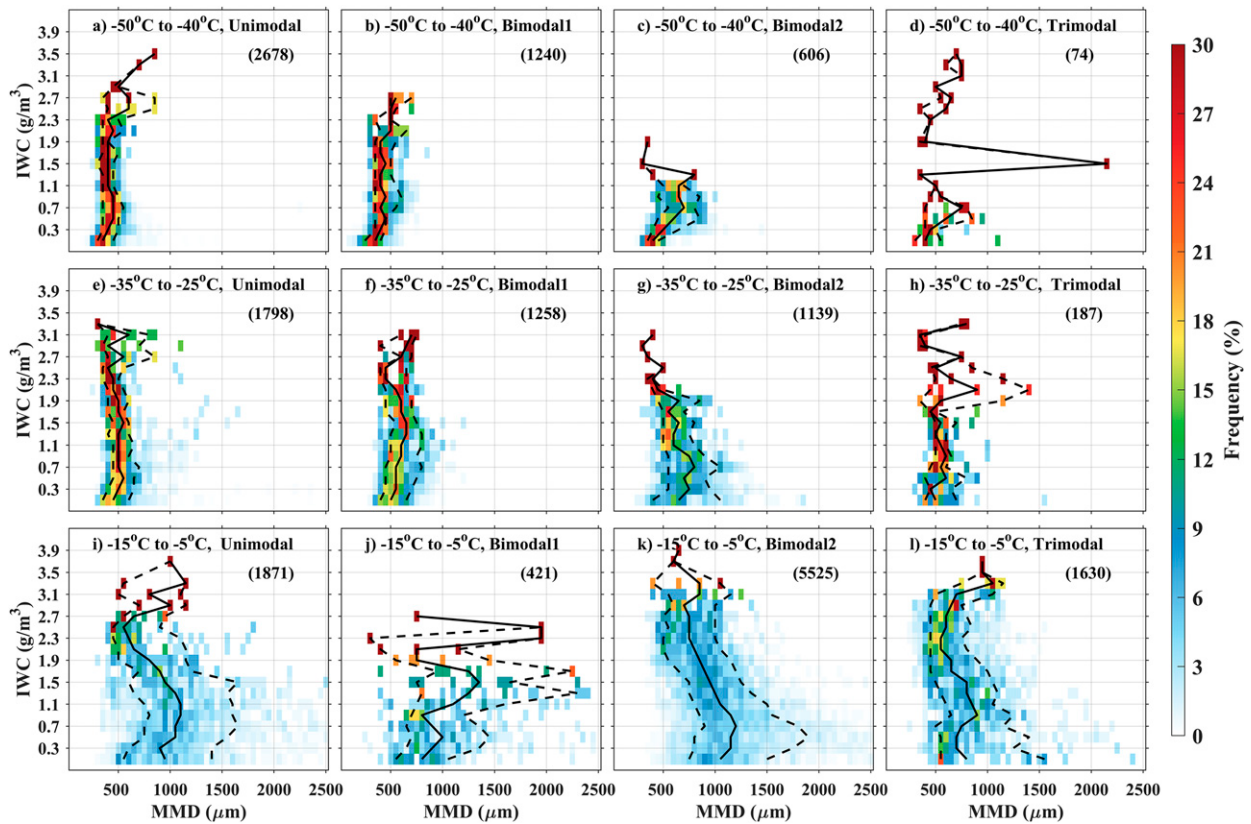


FIG. 4. Normalized frequency of MMD for each IWC range for (a) Unimodal PSDs, (b) Bimodal1 PSDs, (c) Bimodal2 PSDs, and (d) Trimodal PSDs for $-50^{\circ} \leq T \leq -40^{\circ}\text{C}$. (e)–(h) As in Figs. 4a–d, but for $-35^{\circ} \leq T \leq -25^{\circ}\text{C}$. (i)–(l) As in Figs. 4a–d, but for $-15^{\circ} \leq T \leq -5^{\circ}\text{C}$. For each subplot, middle solid line indicates 50th percentile, whereas left and right dashed lines represent 15th and 85th MMD, respectively. Numbers in parentheses give numbers of sample data points.

Measuring Systems (PMS) Forward Scattering Spectrometer Probe (FSSP-100; 2–47 μm), SPEC Cloud Particle Imager (CPI) with 2.3 μm pixel resolution, were used for further PSD characterization, and an Aventech Aircraft Integrated Meteorological Measurements System (AIMMS-20) measured temperature, static pressure, and wind at the flying levels. Licor hygrometer probes model 6262 and model 840A were used to measure water vapor mixing ratio and calculate relative humidity and ice supersaturation following Korolev and Isaac (2006). More information on the use of these probes for these flight campaigns can be found in Strapp et al. (2020).

c. In situ observations of PSDs

Different definitions of particle size have been used to characterize PSDs. These include the maximum dimension (D_{\max}) (e.g., Mitchell and Arnott 1994; McFarquhar and Heymsfield 1996; 1998; McFarquhar and Black 2004; Heymsfield et al. 2013; Jackson et al. 2014; Korolev et al. 2014; Korolev and Field 2015), the area-equivalent diameter (Locatelli and Hobbs 1974; Korolev et al. 2014; Waitz et al. 2021), and the mass-equivalent diameter (Seifert and Beheng 2006). D_{\max} is used to characterize particle size because this parameter has been used in most previous studies that examined observed

ice particle size distributions. Further parameterizations for mass and terminal fall speed that are used in models are usually formulated in terms of maximum dimension. Thus, the use of maximum dimension as opposed to the use of an area-equivalent diameter ensures self-consistency in model schemes (McFarquhar and Black 2004). There are several different ways that D_{\max} has been calculated for a two-dimensional image (Locatelli and Hobbs 1974; Brown and Francis 1995; McFarquhar and Heymsfield 1996; Mitchell and Arnott 1994; Korolev and Field 2015; Heymsfield et al. 2013; Wu and McFarquhar 2016). The definition of D_{\max} as the diameter of a minimum enclosing circle for a two-dimensional particle image is used here following Wu and McFarquhar (2016).

A composite PSD was derived from the 2D-S and PIP covering the size range D_{\max} from 55 to 12 845 μm at 10 μm resolution and is used to calculate cloud microphysical parameters (e.g., ice mass content, MMD, N_i) following the techniques described by Hu et al. (2021). The 2D-S was used in the composite distribution for sizes smaller than 800 μm . Likewise, the PIP was used for sizes larger than 1200 μm , and the composite distribution between 800 and 1200 μm is a linear weighted mean of the 2D-S and ice PIP distributions (Leroy et al. 2016b).

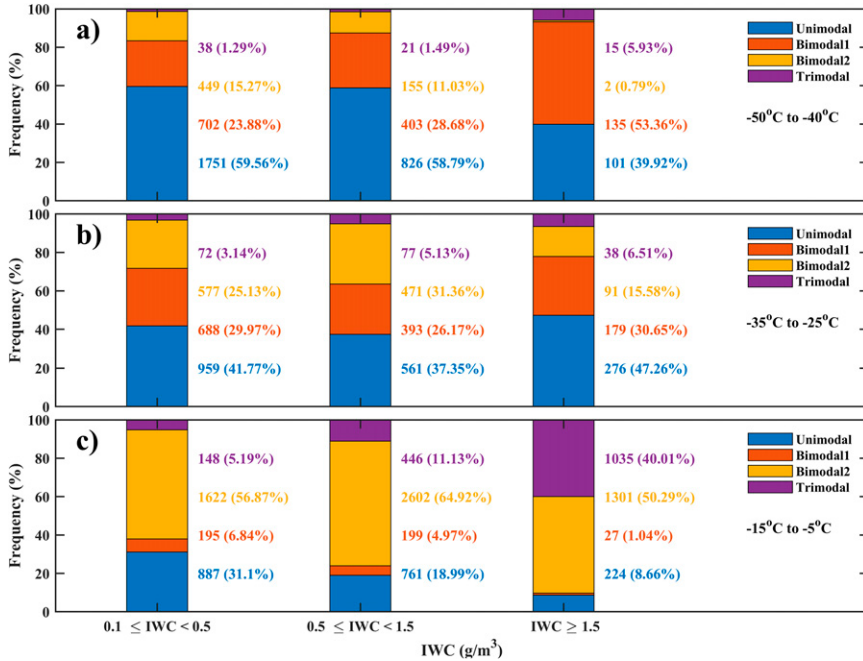


FIG. 5. Normalized occurrence frequency of four different modalities determined by Brechner (2021) algorithm for three IWC ranges for (a) $-50^{\circ} \leq T \leq -40^{\circ}\text{C}$, (b) $-35^{\circ} \leq T \leq -25^{\circ}\text{C}$, and (c) $-15^{\circ} \leq T \leq -5^{\circ}\text{C}$. Blue represents Unimodal PSDs, red represents Bimodal1 PSDs, yellow represents Bimodal2 PSDs, and purple represents Trimodal PSDs. Number of data points and normalized frequency percentage (in parentheses) of each modality labeled for each IWC range in same color as bar. (left) $0.1 \leq \text{IWC} < 0.5 \text{ g m}^{-3}$, (center) $0.5 \leq \text{IWC} < 1.5 \text{ g m}^{-3}$, and (right) $\text{IWC} \geq 1.5 \text{ g m}^{-3}$.

d. Data processing and classifications

Only time periods in ice-phase clouds are examined in this study. Time segments, when the Rosemount Icing Detector frequency was decreasing and was lower than 40 kHz (Mazin et al. 2001) or when N_t measured by the CDP-2 was larger than 10 cm^{-3} (Lance et al. 2010; Ding et al. 2020) identified the presence of liquid water content (LWC) and were removed. This represents only 0.81% of the data obtained by Falcon-20 (Hu et al. 2021). A frequency threshold of 39.7 kHz was applied to the different model of the Rosemount Icing Detector installed on the Convair-580 and showed that 24.7% of the data obtained by the Convair-580 was in liquid conditions. To remove tenuous clouds from analysis, only data with $\text{IWC} \geq 0.1 \text{ g m}^{-3}$ were used for both aircraft. The HIWC regions were defined to occur when the IWC was larger than 1.5 g m^{-3} without any threshold of MMD to use a definition consistent with previous studies (e.g., Leroy et al. 2017; Hu et al. 2021). The IWC and vertical velocity data were averaged over 5-s intervals to match the integration period used for the PSD data. For Falcon-20 flight observations, a total of 12 339 data points representing about 17.2 h of data within organized MCSs were available for analysis, of which 1931 data points were in HIWC regions. A total of 6088 data points representing about 8.5 h of data within organized MCSs were observed by Convair-580, of which 1493 data points were in HIWC region.

To investigate the effects of environmental conditions and other MCS characteristics (e.g., temperature, vertical velocity,

underlying surface characteristics, MCS age, distance away from the convective core) on PSDs, as well as the differences of PSDs between HIWC and other IWC regions, each measurement was classified according to the several environmental characteristics following the methodology of Hu et al. (2021).

e. Methodology

1) IMPROVED IGF TECHNIQUE

The algorithm in Brechner (2021) was used to fit the observed PSDs to a unimodal, bimodal or trimodal gamma distribution. The algorithm automatically identifies the number of modes and the location of each mode for a PSD. The IGF technique developed by McFarquhar et al. (2015) was modified to determine the fit parameters for each mode. To implement the technique, it is first assumed that all PSDs are trimodal, with $N(D_{\max})$, hence, expressed as

$$N(D_{\max}) = N_{o1} \left(\frac{D_{\max}}{D_o} \right)^{\mu_1} e^{-\lambda_1 D_{\max}} + N_{o2} \left(\frac{D_{\max}}{D_o} \right)^{\mu_2} e^{-\lambda_2 D_{\max}} + N_{o3} \left(\frac{D_{\max}}{D_o} \right)^{\mu_3} e^{-\lambda_3 D_{\max}}, \quad (3)$$

where the small, middle, and large modes are represented by subscripts 1, 2, and 3, respectively. For each PSD, a small and large breakpoint is determined. The algorithm determines the number of modes according to the number of breakpoints. If

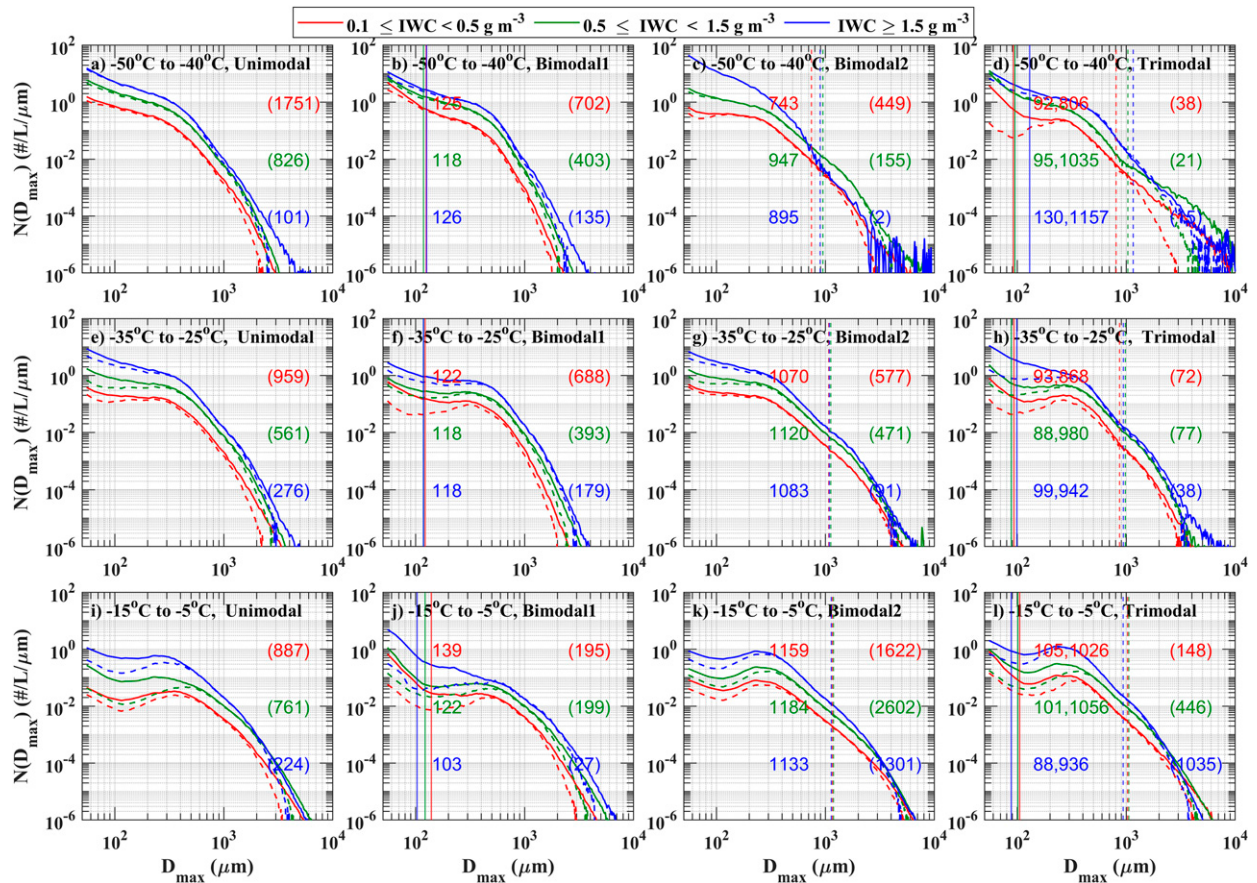


FIG. 6. The mean (solid line) and median (dashed line) distribution of (a) Unimodal, (b) Bimodal1, (c) Bimodal2, and (d) Trimodal PSDs for $-50^\circ \leq T \leq -40^\circ\text{C}$. (e)–(h) As in Figs. 6a–d, but for $-35^\circ \leq T \leq -25^\circ\text{C}$. (i)–(l) As in Figs. 6a–d, but for $-15^\circ \leq T \leq -5^\circ\text{C}$. Red lines indicate $0.1 \leq \text{IWC} < 0.5 \text{ g m}^{-3}$, green lines indicate $0.5 \leq \text{IWC} < 1.5 \text{ g m}^{-3}$, and blue lines indicate $\text{IWC} \geq 1.5 \text{ g m}^{-3}$. For multimodal PSDs, solid vertical lines represent small breakpoints and dashed lines indicate large breakpoints. Values of breakpoints shown in same color as lines. Numbers in parentheses give number of sample data points.

no breakpoint exists, the PSD is unimodal and $N_{o2} = N_{o3} = 0$. If two breakpoints exist, the PSD is trimodal. If only one breakpoint exists, the PSD is bimodal and $N_{o3} = 0$. A breakpoint does not mean that the gamma function for a mode does not characterize crystal sizes larger or smaller, but rather indicates the transition in size at which the dominance of a particular mode changes. Depending on whether the breakpoint is greater than $600 \mu\text{m}$ or less than $200 \mu\text{m}$, the bimodal distribution is called Bimodal1 (small breakpoint $< 200 \mu\text{m}$) or Bimodal2 (large breakpoint $> 600 \mu\text{m}$). Following McFarquhar et al. (2015), the uncertainty in the number of counts in each size bin was considered in determining the fit to the PSD. More details on the development of the scheme are found in Brechner (2021).

Examples of different modality PSDs averaged for different temperature (T) ranges are shown in Fig. 1. The distributions are plotted for different ranges of T because T is the variable that had the biggest impact on microphysical properties for the Cayenne dataset (Hu et al. 2021). Visually, the shapes of the same modality PSD can vary with T because the intercept, slope and shape parameters

can be a function of T . As the generation of particles in different modes is dominated by different processes (small mode by homogeneous nucleation, the large mode by aggregation and sedimentation, and the central mode by riming), the use of three modes should allow better representation of processes in numerical models without the computational expense required by a bin-resolving scheme.

2) PROJECTIONS OF ELLIPSES

An ellipse characterizing the equally realizable solution in (N_o, μ, λ) phase space for each mode was calculated using the algorithm of Moshtagh (2006) that determines a Hessian matrix for the fit phase space for each PSD. A restriction of $-1 < \mu < 10$ and $\lambda > 0$ is applied so that the parameterized PSDs can easily be integrated when incorporated into model parameterization schemes. To construct a volume of equally realizable solutions for a family of PSDs measured in similar environmental conditions, all points contained within 1% of the individual PSD ellipsoids in the family are included. The detailed methodology for determining these ellipsoids is found in McFarquhar et al. (2015).

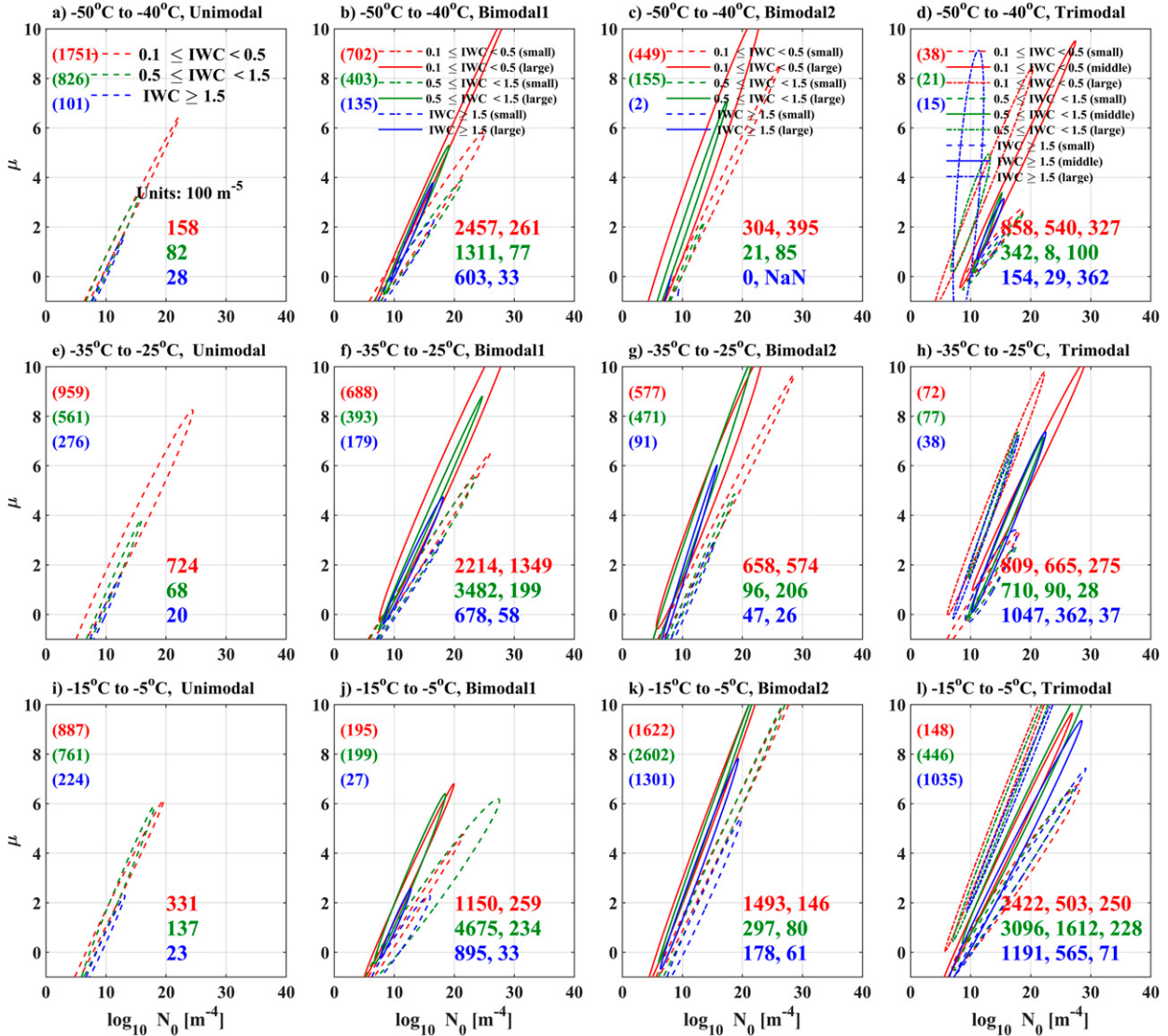


FIG. 7. Projection of three-dimensional ellipses characterizing distributions of equally realizable solutions for fit parameters in (N_o , μ) phase space for (a) Unimodal, (b) Bimodal1, (c) Bimodal2, and (d) Trimodal PSDs at $-50^\circ \leq T \leq -40^\circ\text{C}$. (e)–(h). As in Figs. 7a–d, but for $-35^\circ \leq T \leq -25^\circ\text{C}$. (i)–(l) As in Figs. 7a–d, but for $-15^\circ \leq T \leq -5^\circ\text{C}$. Red lines indicate $0.1 \leq \text{IWC} < 0.5 \text{ g m}^{-3}$, green lines indicate $0.5 \leq \text{IWC} < 1.5 \text{ g m}^{-3}$, and blue lines indicate $\text{IWC} \geq 1.5 \text{ g m}^{-3}$. Different line types represent projections of parameters for different modes in PSDs. Numbers in parentheses give number of sample data points. The volumes of ellipsoid are denoted by colorful numbers and shown in bottom-right corner of each subplot (units: 100 m^{-5}). Unimodal PSDs have one column, Bimodal PSDs have two columns, and Trimodal PSDs have three columns. The number of columns from left to right represents the mode from small to large. For each column, (top) $0.1 \leq \text{IWC} < 0.5 \text{ g m}^{-3}$, (middle) $0.5 \leq \text{IWC} < 1.5 \text{ g m}^{-3}$, and (bottom) $\text{IWC} \geq 1.5 \text{ g m}^{-3}$.

3) OVERLAP PERCENTAGE

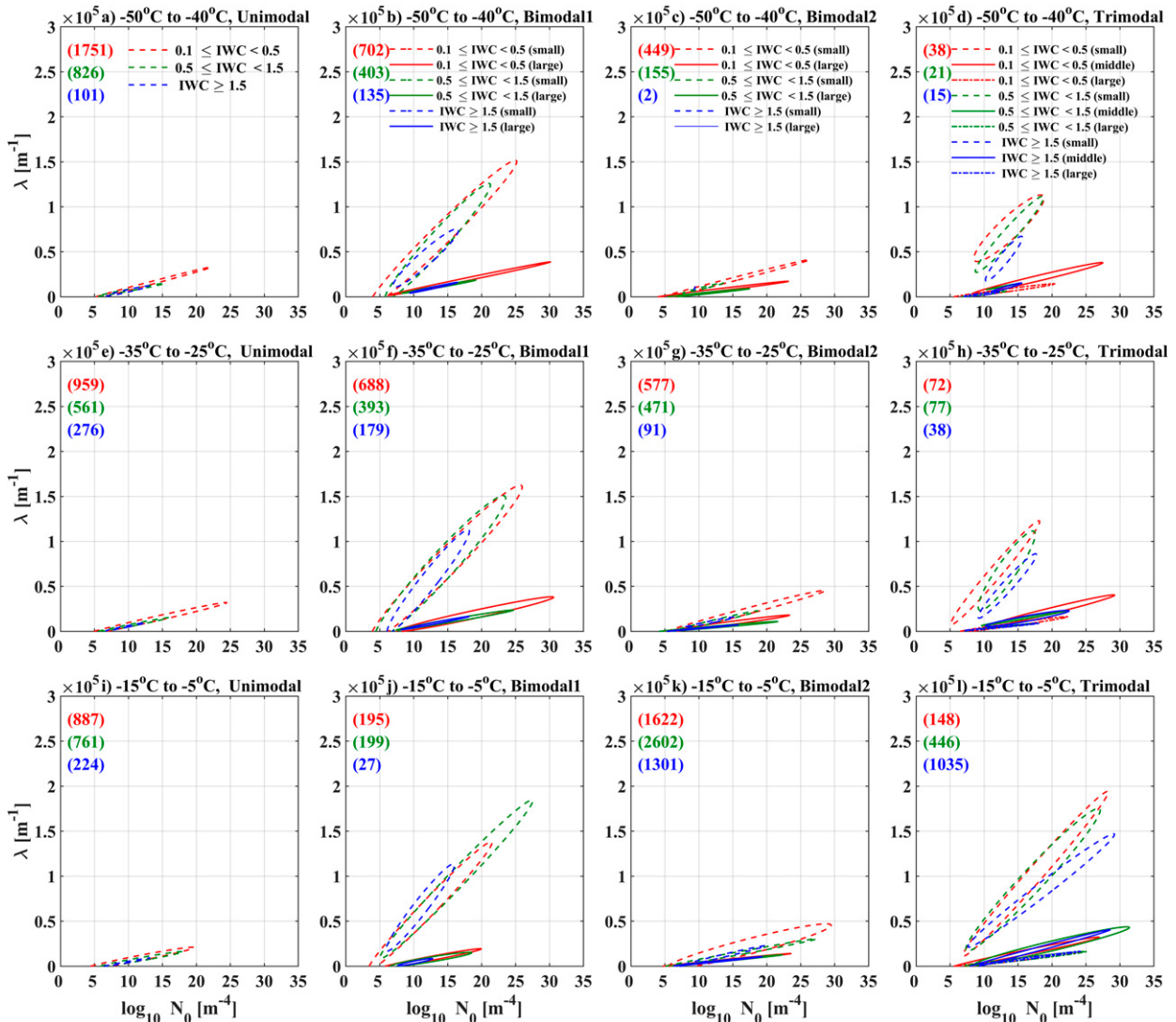
To determine how fit parameters vary with environmental conditions, a three-dimensional volume encompassing two ellipsoids ($S1$, $S2$) describing different environmental conditions is determined (Finlon et al. 2019; Mascio et al. 2020), where N_{s1} and N_{s2} are the number of points inside the $S1$ and $S2$ ellipsoids, respectively, and N_{s0} is the number of points inside both the $S1$ and $S2$ ellipsoids. The ratio (N_{s0}/N_{s1}) of the equally plausible solutions mean number found in both ellipsoids to the number of points in the

$S1$ ellipsoid and represents the overlap percentage, with (N_{s0}/N_{s2}) representing the same for the $S2$ ellipsoid.

3. The distribution of four kinds of modality PSDs

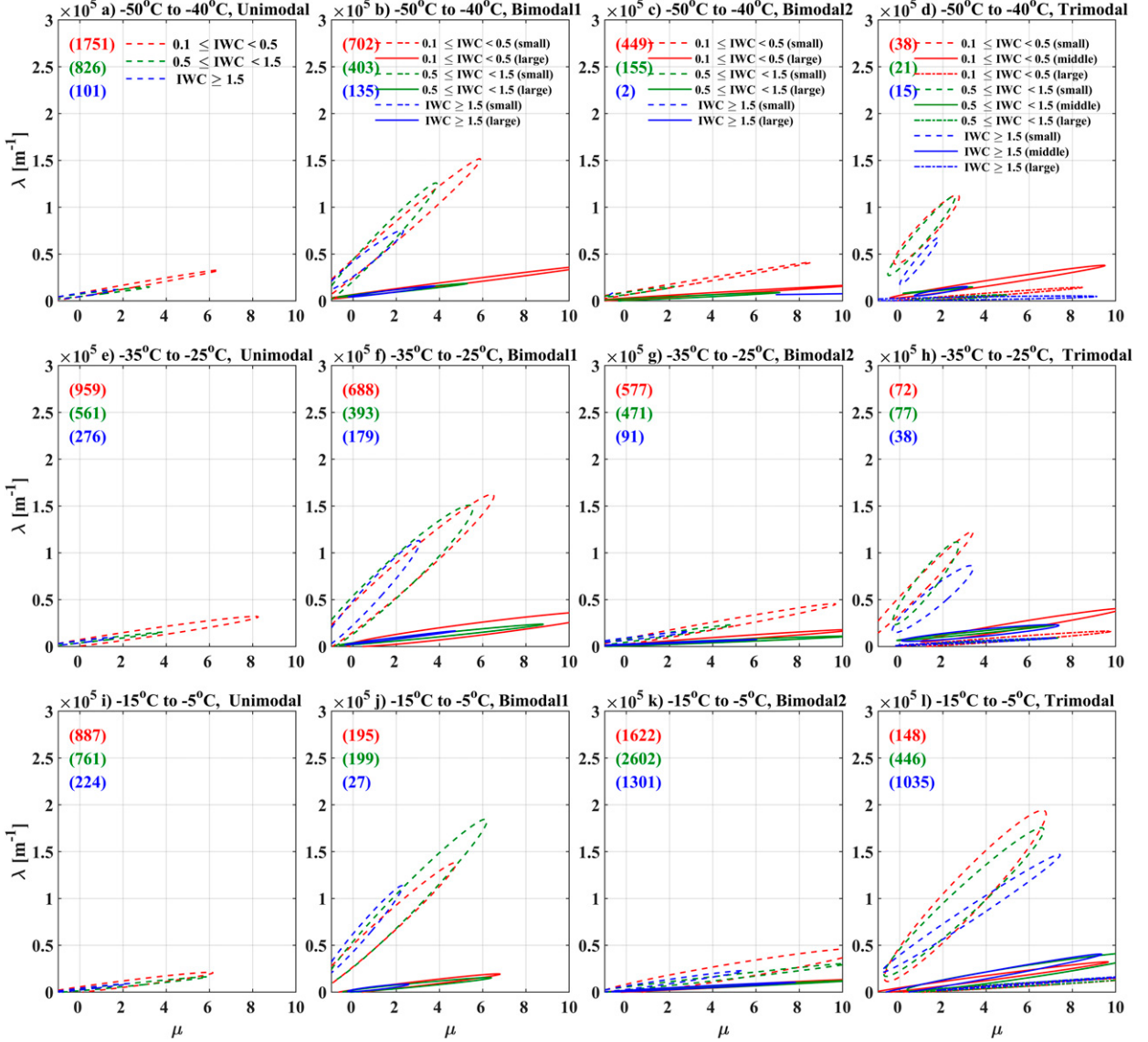
a. Case study

Figure 2 shows a time series of microphysical properties measured by probes on the Convair-580 between 1001:07 and 1154:37 UTC 26 May 2015. The Convair-580 flew at a constant T of $\sim -10^\circ\text{C}$ within an organized Oceanic MCS (Fig. 2a).

FIG. 8. As in Fig. 7, but for (N_o, λ) phase space.

Representative ice crystals measured by the SPEC CPI shown in Figs. 3a–e correspond to P1 (1005:57–1006:37 UTC), P2 (1105:32–1106:47 UTC), P3 (1119:27–1120:32 UTC), P4 (1134:17–1135:22 UTC), and P5 (1152:52–1154:12 UTC) in the morning of 26 May 2015 in Fig. 2c. Typical ice crystals measured by SPEC CPI in Fig. 3f correspond to P6 (1608:27–1609:27 UTC; figure not shown) in the afternoon of 26 May 2015. The mean IWC and MMD are 2.34 g m^{-3} and $738.8 \mu\text{m}$, respectively, during P1, with some columns observed, similar to the ice crystals shapes in Fig. 3f measured during P6, with mean IWC and MMD are 1.65 g m^{-3} and $432.2 \mu\text{m}$, respectively. Thus, for this flight small columns dominated the mass content of the HIWC regions with small MMD ($<500 \mu\text{m}$ at -10°C), with some large ice crystals being aggregates of columns. The mean IWC reaches 2.53 g m^{-3} during P2 and the mean MMD is $959.5 \mu\text{m}$, with the large ice crystals being aggregates of columns and plate-like crystals (Fig. 3b). Similar IWCs have different MMD for P1 and P2,

consistent with the larger ice supersaturation in P2 (~ 0.028) compared to P1 (~ 0.008), making the P2 environment more favorable for the growth of ice crystals (Bailey and Hallett 2009). Besides, the capped column, a column with a plate at either end is observed in P2, suggesting the particle passed through several different growth regimes during its history. The MMD reaches $1880 \mu\text{m}$ when the IWC is 0.42 g m^{-3} during P3, consistent with the large crystal with broad branches shown in Fig. 3c. These crystals are typically formed at temperatures around -15°C at supersaturations greater than those at which plates form. However, ice supersaturation is ~ -0.025 here, consistent with these ice crystals forming in other areas with higher relative humidity condition and falling into this region with transport by the horizontal wind. P4 with low mean IWC 0.27 g m^{-3} and MMD $597.3 \mu\text{m}$, has many small plate crystals (Fig. 3d). Some short and thick capped columns are seen here, different from the long and thin capped columns in P2, consistent with the very low ice supersaturations. A region with lower IWC ($\sim 0.21 \text{ g m}^{-3}$) and

FIG. 9. As in Fig. 7, but for (λ, μ) phase space.

large MMD ($\sim 1262 \mu\text{m}$) found during P5 has plentiful aggregates (Fig. 3e). Many small irregular ice crystals are also found in these six periods. In general, the processes of sedimentation, aggregation, mixing due to shear, vertical wind and horizontal wind transport complicate the analysis because the environment where ice particles are observed does not necessarily represent the environment in which the particles formed or grew. The mixed phase region may also potentially affect the formation of ice crystals. Mixing of air masses with different crystal populations is also very important. Future analysis should try to distinguish between these possibilities by using observations in combination with trajectory analysis and large-eddy simulation (LES) modeling studies. HIWC with small MMD regions are full of small columns and irregular ice crystals, consistent with a negative correlation between IWC and MMD (Leroy et al. 2016a; Hu et al. 2021).

Figure 2d shows a time series of IWC and MMD with the shading indicating the modality of the PSD. Trimodal (sky blue) and Bimodal2 PSDs (green) occur most frequently in HIWC regions. For example, during P2 when $\text{IWC} > 1.5 \text{ g m}^{-3}$, the modality of PSDs is trimodal. When IWC decreases to less than 1.5 g m^{-3} at 1106:57 UTC, the modality becomes Bimodal2 (green) and Unimodal (orange). After 1109:07 UTC when $\text{IWC} > 1.5 \text{ g m}^{-3}$, Trimodal PSDs again dominate. A negative correlation coefficient of -0.2 between IWC and MMD exists for the whole event (1338 samples, Pearson method, p value: 10^{-13}), consistent with small columns and irregular ice crystals dominating the mass of HIWC regions. Figure 2a shows HIWC regions can be as far away from the convective core as 100 km for the leg at -10°C (e.g., $L > 100 \text{ km}$ during P1), suggesting particles were generated in the convective

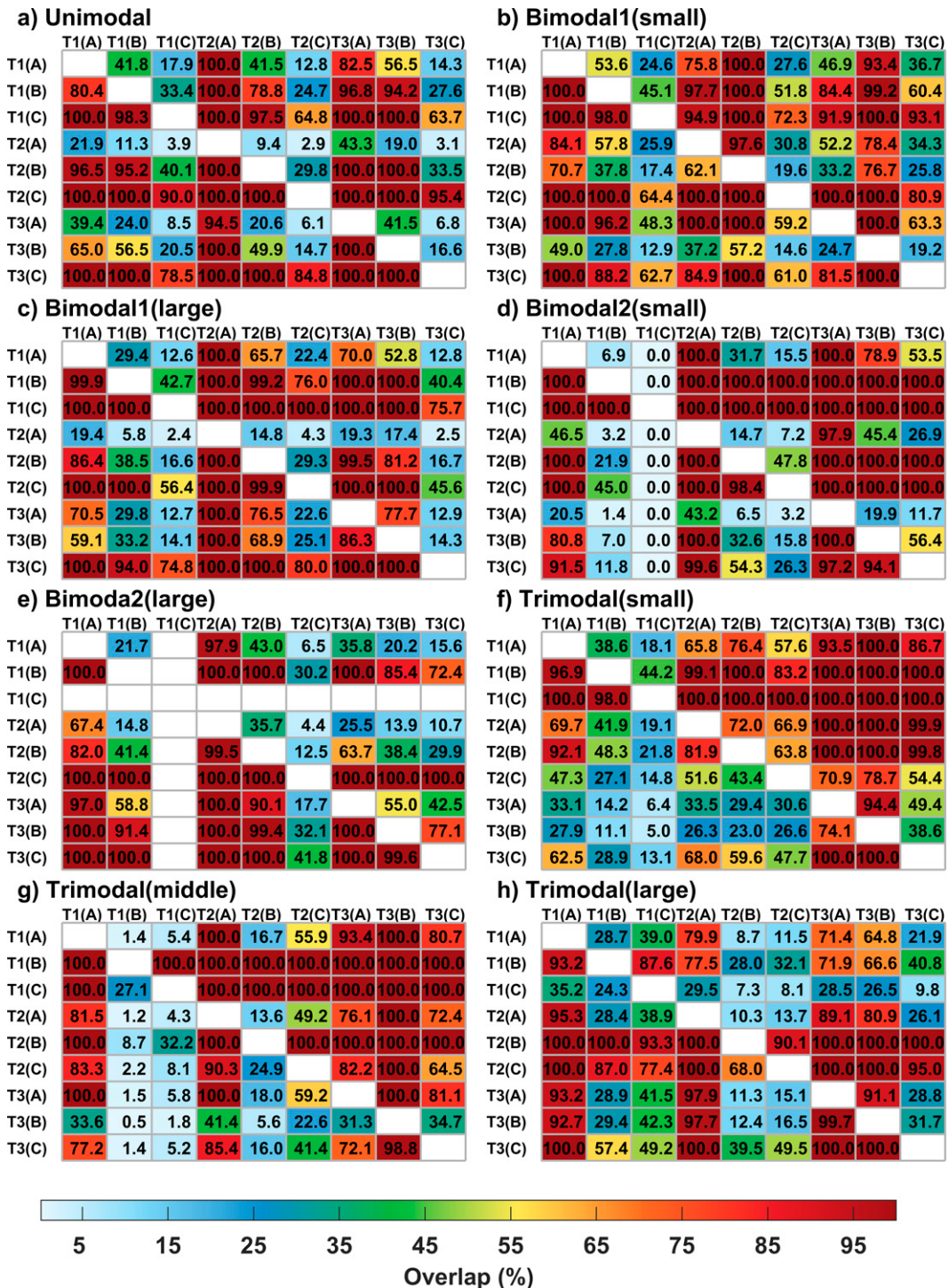


FIG. 10. Matrix of percentage overlap between three-dimensional volumes of equally realizable fit parameters for (a) Unimodal, (b) first mode in Bimodal1, (c) second mode in Bimodal1, (d) first mode in Bimodal2, (e) second mode in Bimodal2, (f) first mode in Trimodal, (g) second mode in Trimodal, and (h) third mode in Trimodal PSDs as function of IWC and T . A represents regions with $0.1 \leq \text{IWC} < 0.5 \text{ g m}^{-3}$, B represents regions with $0.5 \leq \text{IWC} < 1.5 \text{ g m}^{-3}$, and C represents regions with $\text{IWC} \geq 1.5 \text{ g m}^{-3}$. T1, T2, and T3 represent $-50^\circ \leq T \leq -40^\circ\text{C}$, $-35^\circ \leq T \leq -25^\circ\text{C}$, and $-15^\circ \leq T \leq -5^\circ\text{C}$, respectively. Boxes colored according to percentage overlap. For example, green box in first row and second column of (a) means 41.8% of the equally plausible solutions found in $-15^\circ \leq T \leq -5^\circ\text{C}$ and $0.1 \leq \text{IWC} < 0.5 \text{ g m}^{-3}$ family are also found in $-15^\circ \leq T \leq -5^\circ\text{C}$ and $0.5 \leq \text{IWC} < 1.5 \text{ g m}^{-3}$ family.

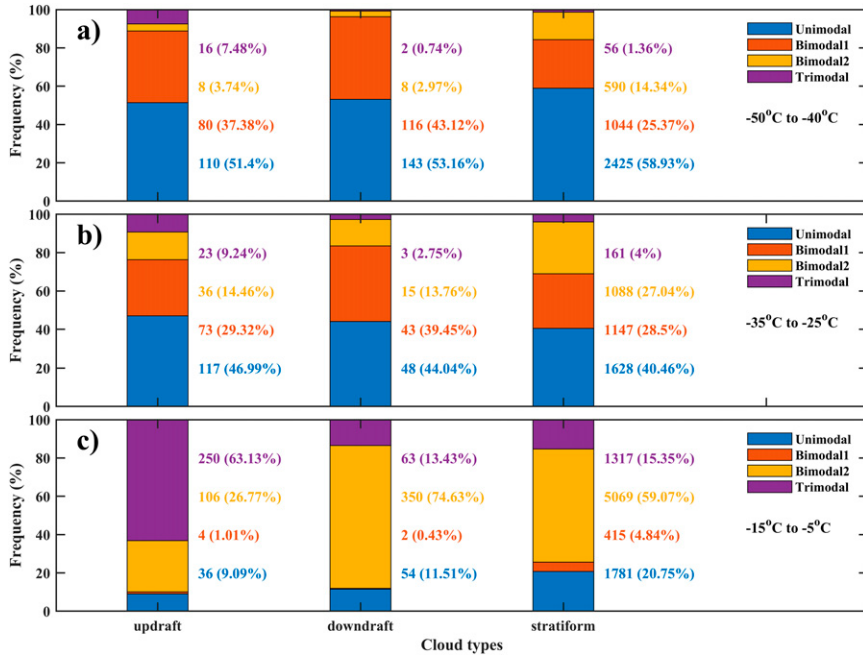


FIG. 11. As in Fig. 5, but for updrafts, downdrafts, and stratiform regions.

core and then transported and fell into this region (Hu et al. 2021). The lack of response from the Rosemount Icing Detector (Fig. 2f) and the $N_t < 10 \text{ cm}^{-3}$ measured by the CDP-2 (Fig. 2g) after 1110:00 UTC confirm that most of these data were collected in ice clouds. However, even though mixed phase regions were excluded from the analysis, many of the ice crystals observed could have formed or grew in mixed-phase regions. The N_t measured by the 2D-S and PIP (Fig. 2h) are usually larger for Trimodal PSDs (sky blue) and Bimodal2 PSDs (green) showing these regions are full of small ice crystals and a positive correlation coefficient of 0.65 between IWC and N_t (Pearson method, p value: 10^{-165}) exists during the whole event.

b. Distributions of MMD for different modality PSDs

To investigate how MMD depends on the PSD modality, the normalized frequency of MMD for each IWC range for Unimodal, Bimodal1, Bimodal2, and Trimodal PSDs as a function of T is shown in Fig. 4. The ranges of MMD decrease sharply with decreasing T , consistent with the analysis of Hu et al. (2021). The increase of MMD with T is consistent with growth by vapor deposition and aggregation (Mitchell 1996). Increased contributions from sedimentation as larger particles fall to lower altitudes is one of the most important factors (Jackson et al. 2015). For different modality PSDs at the same T , MMDs for Bimodal2 and Trimodal PSDs are larger than those for Unimodal and Bimodal1 PSDs for $T \leq -25^\circ\text{C}$, but trends for $-15^\circ \leq T \leq -5^\circ\text{C}$ are different. The median MMD in Unimodal PSDs increases with IWC to about $1000 \mu\text{m}$ at an IWC of 1.0 g m^{-3} (Fig. 4i), but sharply decreases thereafter for $\text{IWC} > 1.0 \text{ g m}^{-3}$. Different trends for MMD for Bimodal1 and Bimodal2 PSDs are seen in Fig. 4j and Fig. 4k, with MMD increasing with IWC for Bimodal1 PSDs and

decreasing for Bimodal2 PSDs. The median MMD is approximately constant ($\sim 800 \mu\text{m}$) when $\text{IWC} < 1.5 \text{ g m}^{-3}$ for Trimodal PSDs (Fig. 4l), and MMD is the smallest when IWC is around 2.3 g m^{-3} . This suggests the number of large ice crystals increases as IWC increases for Bimodal1 PSDs, and the number of small ice crystals increases as IWC increases for other three types of PSDs.

4. $N(D)$ as a function of environmental conditions

In this section, the characteristics of the functional fits of the observed PSDs are examined as a function of environmental conditions (e.g., cloud types, underlying surface characteristics, MCS ages and distance away from the convective core). As T primarily influences the distributions of IWC and MMD (Hu et al. 2021), PSDs were first sorted into three T ranges ($-15^\circ \leq T \leq -5^\circ\text{C}$; $-35^\circ \leq T \leq -25^\circ\text{C}$; $-50^\circ \leq T \leq -40^\circ\text{C}$) before examining the influence of other environmental conditions. Most of the data were collected at three different constant altitude legs at T of -10° , -30° , and -45°C .

a. Different IWC regions

To compare PSDs in high IWC regions with regions without high IWC, PSDs were sorted into three IWCs ($0.1 \leq \text{IWC} < 0.5 \text{ g m}^{-3}$; $0.5 \leq \text{IWC} < 1.5 \text{ g m}^{-3}$; $\text{IWC} \geq 1.5 \text{ g m}^{-3}$). Figure 5 shows the normalized frequency of occurrence of the four different modality PSDs for the three IWC ranges as a function of T . It is apparent that the modality of PSDs is strongly dependent on T and is related to IWC, the frequency of multimodal PSDs increases with T , and the frequency of Unimodal PSDs decreases with T . For example, the frequency of Unimodal PSDs can be larger than

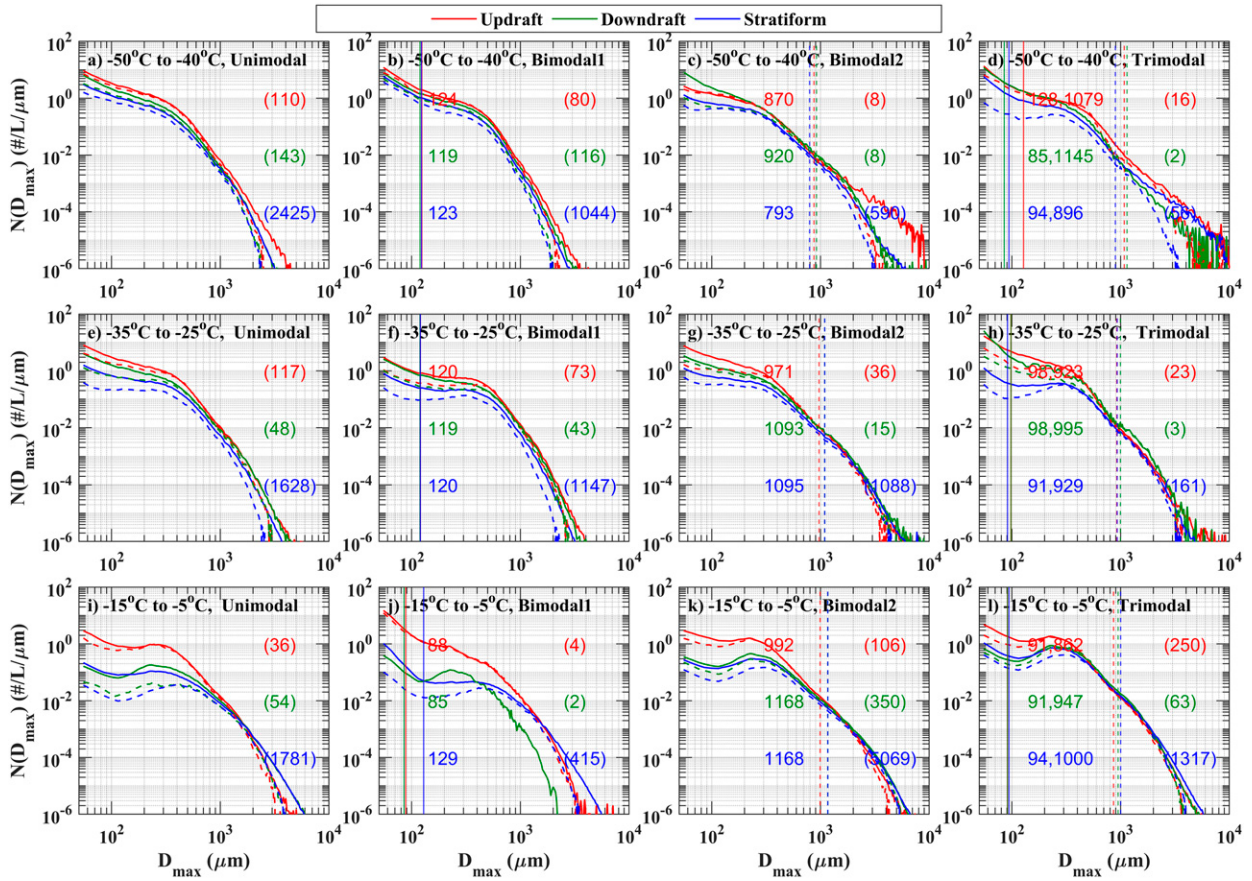


FIG. 12. As in Fig. 6, but segregated according to whether observations obtained in updrafts, downdrafts, or stratiform regions.

50% for IWC < 1.5 g m⁻³ when $-50^\circ \leq T \leq -40^\circ\text{C}$ (Fig. 5a), but decreases to less than 32% when $-15^\circ \leq T \leq -5^\circ\text{C}$ (Fig. 5c). This is consistent with small ice crystals experiencing aggregation when falling from higher to lower altitude, and heterogeneous nucleation in the presence of particles descending from the higher altitude (Zhao et al. 2010), leading to the varying shapes of PSDs and frequency of modality of PSDs with T . The changes of modality with IWC are strongly dependent on T . For $-15^\circ \leq T \leq -5^\circ\text{C}$ (Fig. 5c), the frequency of Unimodal PSDs decreases from ~31% to ~8.7% with increasing IWC, while the frequency of Trimodal PSDs increases from ~5.2% to ~40%. The frequency of Bimodal2 PSDs increases with increasing IWC for $-15^\circ \leq T \leq -5^\circ\text{C}$, but the frequency of Bimodal1 PSDs decreases with increasing IWC. However, for $-35^\circ \leq T \leq -25^\circ\text{C}$ and $-50^\circ \leq T \leq -40^\circ\text{C}$ (Figs. 5a,b), the frequency of PSDs modalities does not show obvious changes with increasing IWC. In summary, the frequency of Unimodal PSDs decreases and the frequency of multimodal PSDs increases with increasing T , and different trends for the frequency of the modality of PSDs with varying IWC for different T exist.

Figure 6 shows the mean (solid line) and median (dashed line) distributions of PSDs for different IWC regions as a function of T , with breakpoints between modes marked. The shapes of PSDs can change a lot even for the same modality with the changes heavily dependent on T . The N_r of small ice

crystals (<200 μm) decreases with increasing T , consistent with MMD increases with increasing T and a negative correlation between T and N_r (Jackson et al. 2015; Hu et al. 2021). This is consistent with ice crystals experiencing more aggregation and sedimentation at lower altitudes. Small ice crystals can completely evaporate in subsaturated environments to keep the concentrations of ice crystals with $D_{\max} < 100 \mu\text{m}$ relatively low (Korolev et al. 2011, 2013). There are usually more small ice crystals (<200 μm) and fewer large ice crystals ($D_{\max} > 2000 \mu\text{m}$) as IWC increases for Bimodal2 and Trimodal modality at the same T , which is consistent with the MMD being negatively correlated with IWC. However, for Bimodal1 PSDs, the opposite trend can be seen (Figs. 6b,f,j), as both the number of small and large ice crystals increase with increasing IWC, which is consistent with the MMD being positively correlated with IWC for $-15^\circ \leq T \leq -5^\circ\text{C}$ (Fig. 4j) and the MMD being constant for $-35^\circ \leq T \leq -25^\circ\text{C}$ and $-50^\circ \leq T \leq -40^\circ\text{C}$ (Figs. 4b,f). The breakpoint between the two modes for Bimodal1 PSDs averages $120 \pm 20 \mu\text{m}$ and exhibits little dependence on T . Even though this breakpoint occurs over a size range where the sample volume of the optical array probes is rapidly increasing with particle size (Baumgardner et al. 2017; McFarquhar et al. 2017), the existence of the bimodal distribution does not appear to be instrument related because the bimodal distributions do not occur

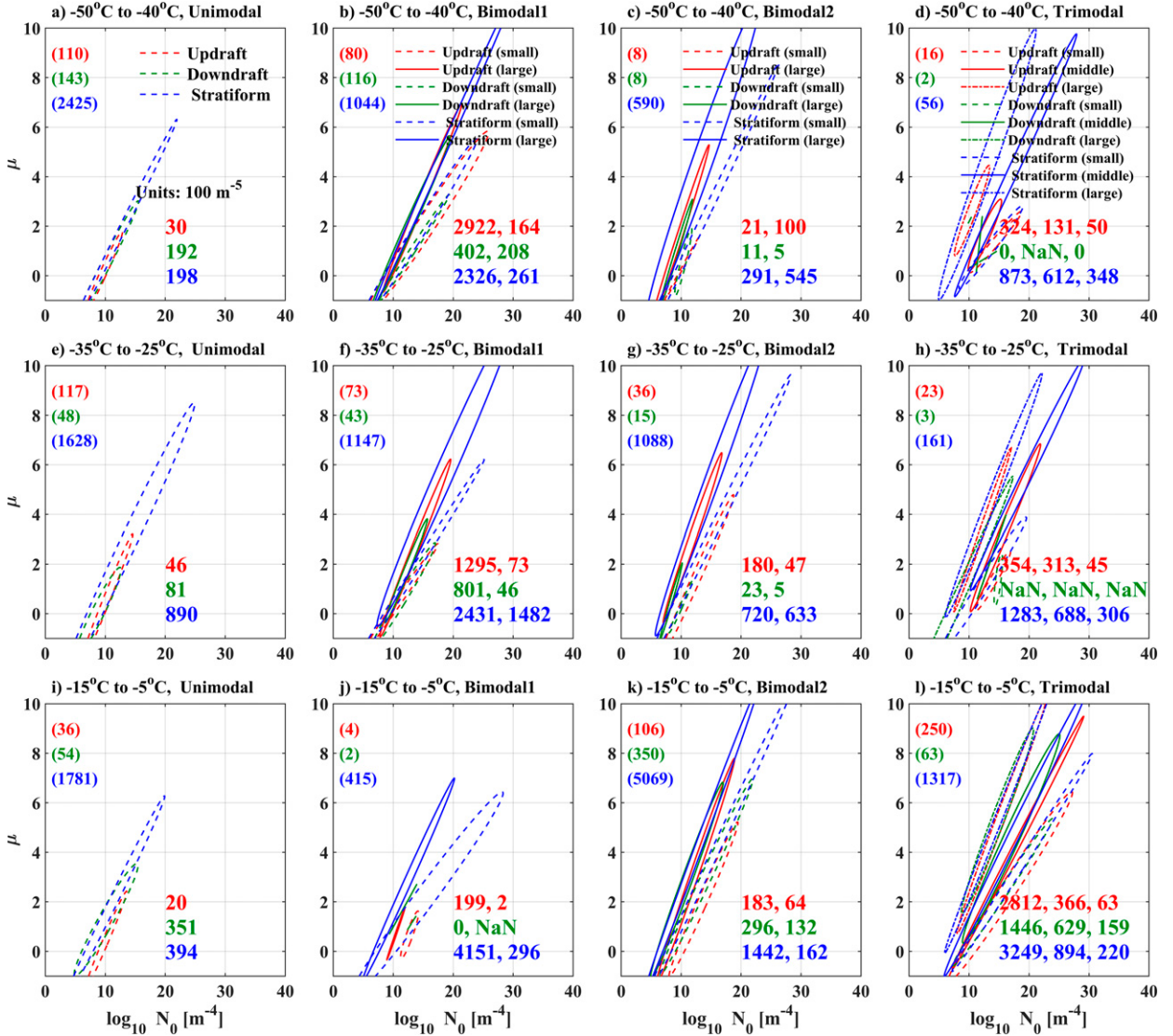


FIG. 13. As in Fig. 7, but segregated according to whether observations obtained in updrafts, downdrafts, or stratiform regions. Different line types represent projections of parameters for different modes in PSDs. Numbers in parentheses give the number of sample data points. The volumes of ellipsoid are denoted by colorful numbers and are shown in bottom-right corner of each subplot. Unimodal PSDs have one row, Bimodal PSDs have two rows, and Trimodal PSDs have three rows. The number of columns from left to right represents the mode from small to large. For each column, (top) updrafts, (middle) downdrafts, and (bottom) stratiform regions.

all the time. The mean breakpoints between the two modes for bimodal2 PSDs range between 743 and 1184 μm , with the breakpoints typically increasing with T , and minimal dependence on IWC. For the Trimodal PSDs, the mean breakpoints between the small mode and middle mode range from 88 to 130 μm , and the mean breakpoints between the middle mode and large mode range from 806 to 1157 μm . The mean breakpoints increase with increasing T for the regions with $0.1 \leq \text{IWC} < 0.5 \text{ g m}^{-3}$ and decrease with increasing T for the HIWC regions with $\text{IWC} \geq 1.5 \text{ g m}^{-3}$. The small breakpoints and large breakpoints in Trimodal PSDs correspond to the breakpoints in the Bimodal1 PSDs and the breakpoints in Bimodal2 PSDs, respectively.

To construct volumes of equally realizable solutions characterizing a family of PSDs, McFarquhar et al. (2015) defined a single ellipsoid around all $(N_o - \lambda - \mu)$ contained within at least 1% of the volumes for the PSDs contained within a family. The volumes characterizing the different modes in PSDs were similarly defined for each mode separately. To visualize the relationship of the gamma fit parameters with IWC as a function of T , two-dimensional projections of the volumes in (N_o, μ) phase space are shown in Fig. 7. Different color lines represent different IWC groups, and different types of lines represent the distribution of parameters for the different modes. Regardless of the modality, μ is directly correlated with and increases with N_o . The slopes of the long axis of the ellipse in

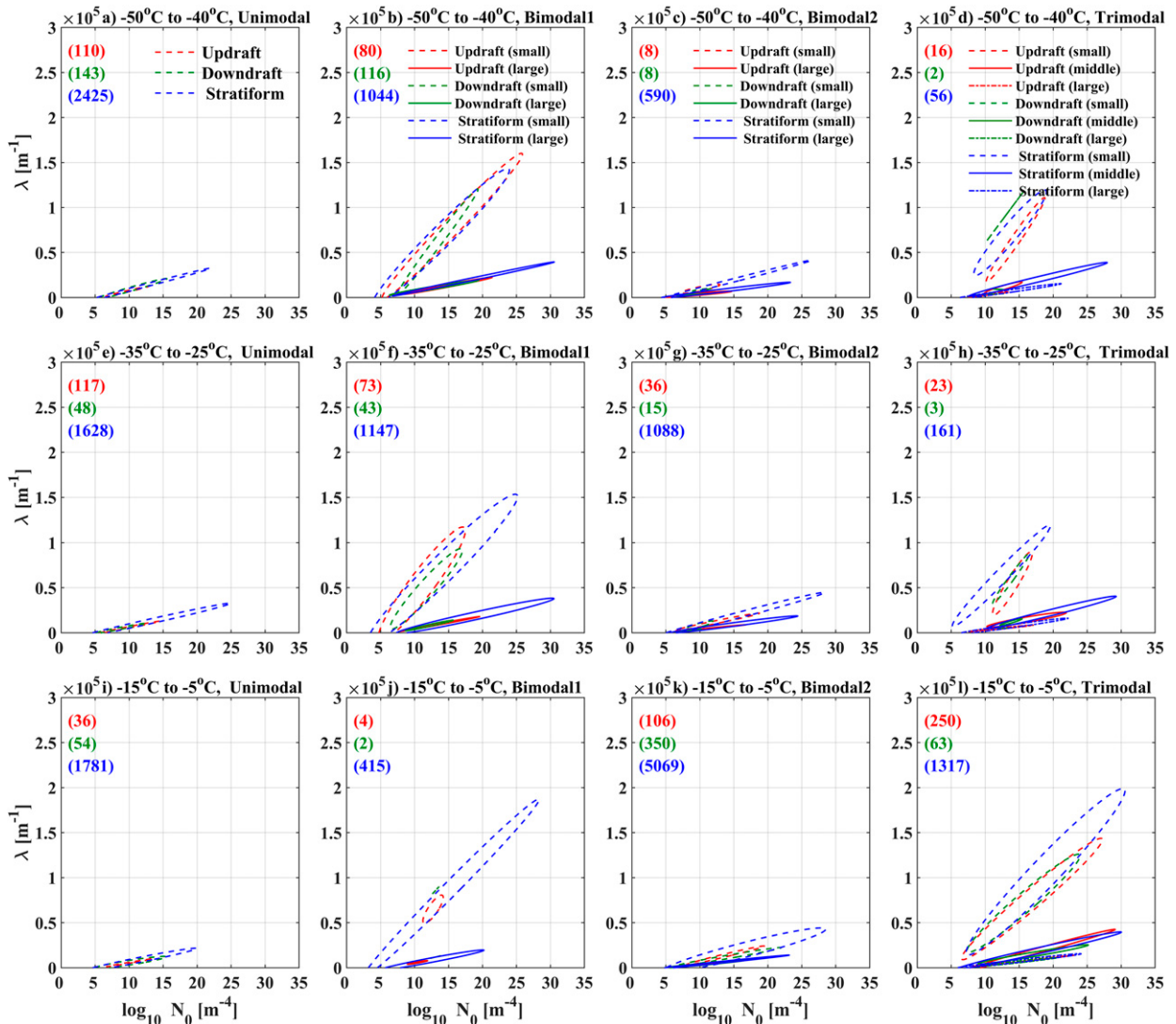


FIG. 14. As in Fig. 8, but segregated according to whether observations are obtained in updrafts, downdrafts, or stratiform regions.

(N_o, μ) phase space are the largest for the small mode in the Trimodal PSDs, while slopes are smallest for the large mode in the Trimodal PSDs. The slopes of the long axis of the ellipse in (N_o, μ) phase space for Bimodal2 are usually larger than those for Bimodal1. In general, the slopes of the long axis of the ellipse in (N_o, μ) phase space in multimodal PSDs are larger for the small mode than for the large mode. For the same N_o, μ usually decreases with increasing IWC. For example, N_o decreases from 10^{22} to 10^{14} m^{-4} and the maximum of μ decreases from 6.5 to 1.8 for Unimodal PSDs for increases in IWC from $0.1 \leq \text{IWC} < 0.5 \text{ g m}^{-3}$ to $\text{IWC} \geq 0.5 \text{ g m}^{-3}$ when $-50^\circ \leq T \leq -40^\circ\text{C}$. Consistent with previous findings of Mascio et al. (2020) showing that μ and λ tend to decrease with increasing IWC, this means the volumes of ellipsoids for small IWC regions are usually larger than those for large IWC. For example, at $-50^\circ \leq T \leq -40^\circ\text{C}$, the volume of ellipsoid for $0.1 \leq \text{IWC} < 0.5 \text{ g m}^{-3}$ is $\sim 1.6 \times 10^4 \text{ m}^{-3} \mu\text{m}^{-2}$, while it

decreased to $2.8 \times 10^3 \text{ m}^{-3} \mu\text{m}^{-2}$ when $\text{IWC} > 1.5 \text{ g m}^{-3}$. The smaller μ as IWC increases is consistent with more small ice crystals with increasing IWC, and with MMD decreasing with increasing IWC. The range of N_o is from 10^5 to above 10^{20} m^{-4} , values that cover more than 15 orders of magnitude, consistent with previous studies (e.g., McFarquhar et al. 2015; Jackson et al. 2015; Mascio et al. 2020). In addition, these figures also show that there are less prominent impacts on how T affects the parameters of PSDs.

Figure 8 shows the ellipse distributions in (N_o, λ) phase space for different modes as a function of T and IWC. Regardless of modality, λ increases with N_o . Similar to (N_o, μ) phase space, the slopes of the long axis of the ellipses in (N_o, λ) phase space are largest for the small mode in Trimodal PSDs, and smallest for the large mode in Trimodal PSDs. The slopes of the long axis of the ellipse and values of λ in (N_o, λ) phase space for Bimodal1 PSDs are usually larger than those in Bimodal2

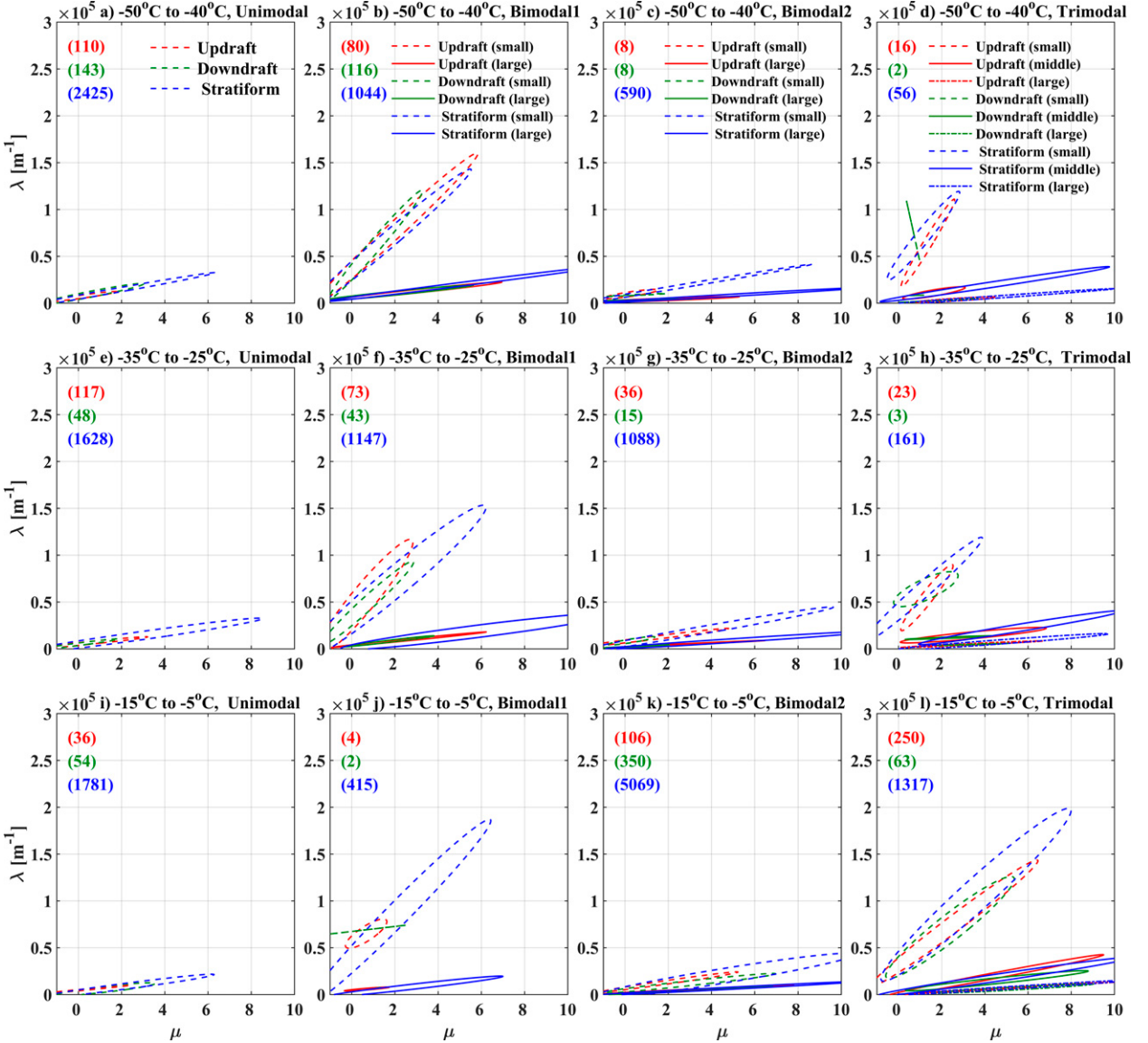


FIG. 15. As in Fig. 9, but segregated according to whether observations are obtained in updrafts, downdrafts, or stratiform regions.

PSDs, due to the existence of more large crystals in the Bimodal2 PSDs. This is expected because the breakpoint occurs at a larger D_{\max} . For the same N_o , there are less obvious changes for λ with increasing T for Unimodal, Bimodal1, and Bimodal2 PSDs, while the range of λ increases for the small mode of Trimodal PSDs. The range of λ tends to be smaller with increasing IWC regardless of the modality of PSDs and the ellipses of small IWCs are usually larger than those of larger IWCs.

Figure 9 shows the ellipse distributions in (μ, λ) phase space. Regardless of modalities, λ increases with increasing μ . Similar to the (N_o, λ) and (N_o, μ) phase spaces, the slopes of the long axis of the ellipse in (μ, λ) phase space are largest for the small mode in the Trimodal PSDs, and smallest for the large mode. The slopes of the long axis of the ellipse in (μ, λ) phase space for Bimodal1 PSDs are usually larger than those

in Bimodal2 PSDs. That means for the same μ , λ is usually smaller in Bimodal2 PSDs than in Bimodal1 PSDs, consistent with the presence of more larger ice crystals in Bimodal2 PSDs due to contributions from processes such as aggregation. Similar to the other projections, there is no strong dependence of the slopes of μ and λ on IWC, but the volumes of the ellipses of small IWCs are usually larger than those of large IWCs.

To develop a size distribution parameterization for use in models and to learn more about processes occurring in these clouds, it is necessary to quantify the dependence of fit parameters on environmental conditions. Figure 10 shows the fractional overlap between the ellipsoids describing the three-dimensional volumes of equally realizable fit parameters for different IWC and T ranges for all four modalities. For

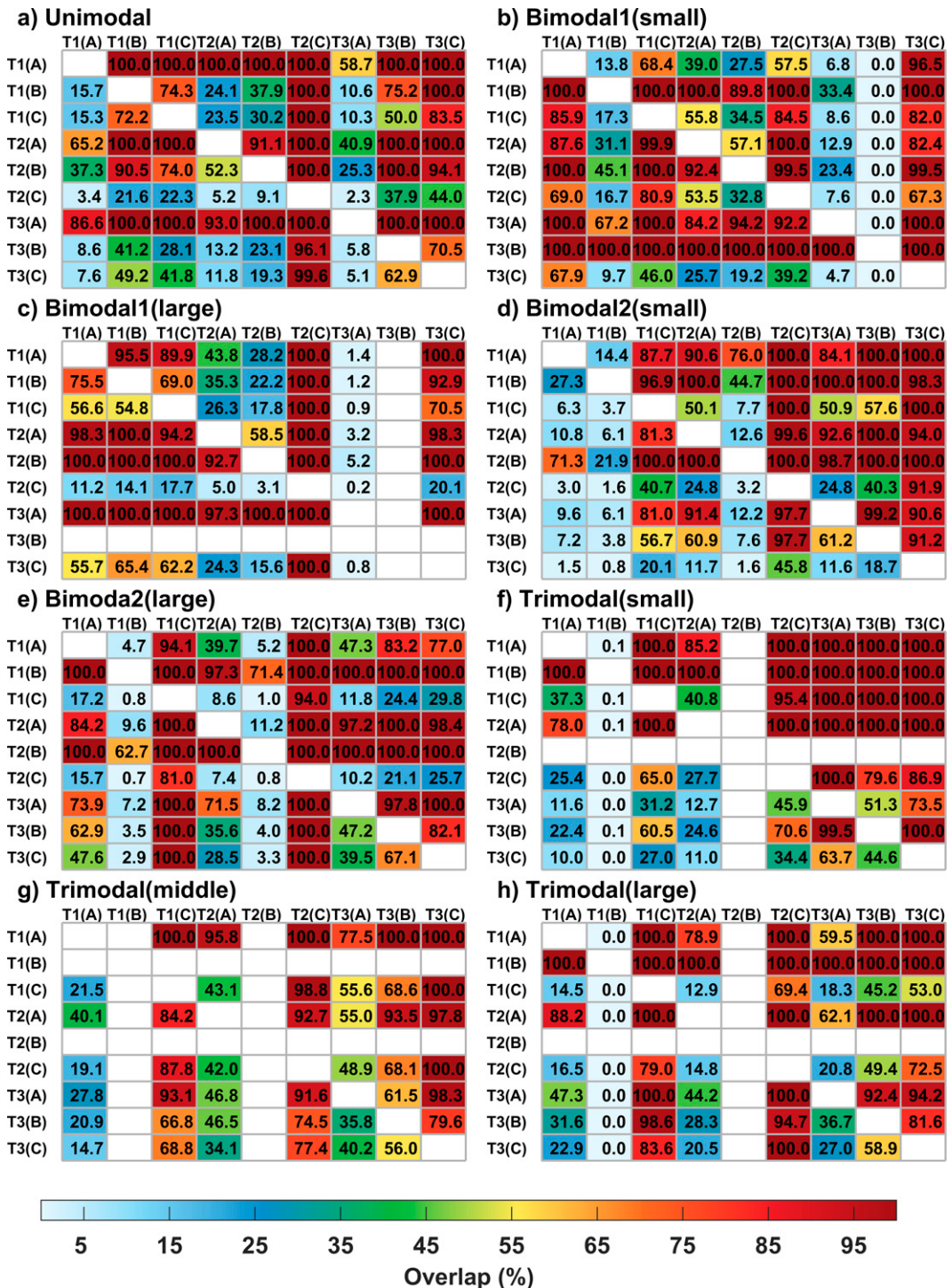


FIG. 16. As in Fig. 10, but for different vertical velocities. A, B, and C represents three cloud types: updrafts, down-drafts, and stratiform regions, respectively. T1, T2, and T3 represent $-50^\circ \leq T \leq -40^\circ\text{C}$, $-35^\circ \leq T \leq -25^\circ\text{C}$, and $-15^\circ \leq T \leq -5^\circ\text{C}$, respectively.

different IWC families at the same T , the volumes in regions with $\text{IWC} \geq 1.5 \text{ g m}^{-3}$ are usually smaller than the regions with $\text{IWC} < 1.5 \text{ g m}^{-3}$ regardless of modality. For example, for the temperature range $-15^\circ \leq T \leq -5^\circ\text{C}$ the blue box in

the first row and third column of Fig. 10a means 17.9% of the equally plausible solutions with $0.1 \leq \text{IWC} < 0.5 \text{ g m}^{-3}$ are found in the family with $\text{IWC} \geq 1.5 \text{ g m}^{-3}$, whereas the dark red box in the third row and first column indicates all

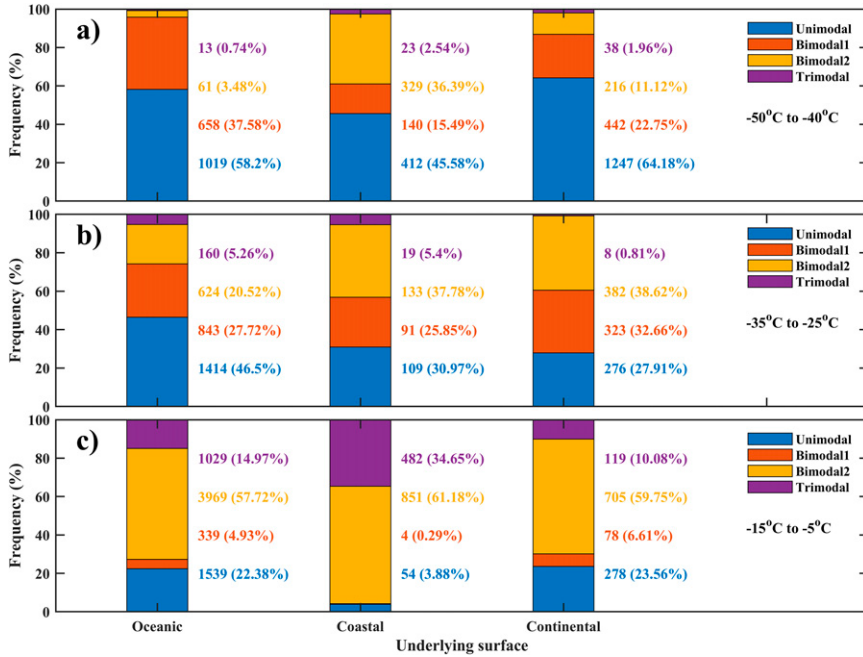


FIG. 17. As in Fig. 5, but segregated according to whether observations are obtained in MCSs over different underlying surface characteristics (land, ocean, or coastal line).

solutions with $IWC \geq 1.5 \text{ g m}^{-3}$ are contained in the family with $0.1 \leq IWC < 0.5 \text{ g m}^{-3}$. The matrices are not symmetric, because the overlap between any two ellipsoids is unique, and each ellipsoid has its own special central position and range. A prominent feature in Fig. 10a is that for the Unimodal PSDs at $-15^\circ \leq T \leq -5^\circ\text{C}$, less than 20% of the equally plausible solutions found in regions with $IWC < 1.5 \text{ g m}^{-3}$ are contained in the families with $IWC \geq 1.5 \text{ g m}^{-3}$ while $\sim 100\%$ of the points in the family with $IWC \geq 1.5 \text{ g m}^{-3}$ are found in the regions with $0.5 \leq IWC < 1.5 \text{ g m}^{-3}$. Similar trends for volume overlap can be seen for Bimodal1 (small) and Bimodal1 (large). In general, the ellipsoids of $0.1 \leq IWC < 0.5 \text{ g m}^{-3}$ families have the largest volumes for all modalities, while volumes for $IWC \geq 1.5 \text{ g m}^{-3}$ families have the smallest volumes. Except for the large mode in Trimodal PSDs, the percentage overlap is usually more than 60% and even up to 100% for regions with $IWC \geq 1.5 \text{ g m}^{-3}$ when $-50^\circ \leq T \leq -40^\circ\text{C}$. This makes sense as the volume of ellipsoid for $-15^\circ \leq T \leq -5^\circ\text{C}$ and $IWC \geq 1.5 \text{ g m}^{-3}$ is usually the smallest, consistent with the ranges of parameters shown in Figs. 7, 8, and 9, indicating that the parameters (N_o , μ , and λ) are constrained for HIWC regions compared to other regions.

In summary, the volumes of the ellipsoids decrease with increasing IWC because there are more small ice crystals in the higher IWC regions. Both λ and μ increase with N_o , and λ increases with increasing μ , consistent with the trends noted by McFarquhar et al. (2007), Heymsfield and McFarquhar (2002), and Heymsfield et al. (2013). And, the N_o , λ , and μ exhibit mutual dependence and are not truly independent parameters, consistent with previous studies (e.g., McFarquhar et al. 2015; Mascio et al. 2020).

b. Vertical velocity

To investigate the impact of vertical motion on PSDs, data were divided according to whether they were obtained in updrafts, downdrafts, or stratiform regions. A convective updraft (downdraft) was defined as any 5-s period when $w > 1 \text{ m s}^{-1}$ ($<-1 \text{ m s}^{-1}$) was sustained for at least four consecutive seconds (Jorgensen et al. 1985; McFarquhar and Black 2004; Murphy et al. 2017). A stratiform region (i.e., $-1 \leq w \leq 1 \text{ m s}^{-1}$) was a period that had neither an updraft nor a downdraft present. Figure 11 shows the normalized frequency of the different modalities for the different vertical motion categories. An apparent feature is that the frequency of Unimodal PSDs at $-50^\circ \leq T \leq -40^\circ\text{C}$ is larger than those at $T \leq -35^\circ\text{C}$ regardless of vertical motion. Further, the frequency of Bimodal2 PSDs and Trimodal PSDs both increase as T increases, while the frequency of Bimodal1 PSDs decreases with increasing T regardless of vertical motion. Despite trends with T dominating any trend with vertical motion, there is still a clear trend in that the frequency of Trimodal PSDs in updrafts is more frequent than for downdrafts or stratiform regions, especially for $-15^\circ \leq T \leq -5^\circ\text{C}$ (Fig. 11c). This is consistent with previously noted trends in IWC (Fig. 5) because the IWCs in updrafts are larger than those in the other areas. The frequency of Bimodal PSDs is the largest ($\sim 75\%$) in downdrafts $-15^\circ \leq T \leq -5^\circ\text{C}$ (Fig. 11c).

Figure 12 shows the mean (solid line) and median (dashed line) PSDs for different vertical velocities as a function of T for all modality PSDs. Consistent with trends in Fig. 11, the PSDs are more dependent on T than on vertical motion. But there is some dependence on vertical motion. There are typically more small ice crystals ($< 500 \mu\text{m}$) in updrafts than in

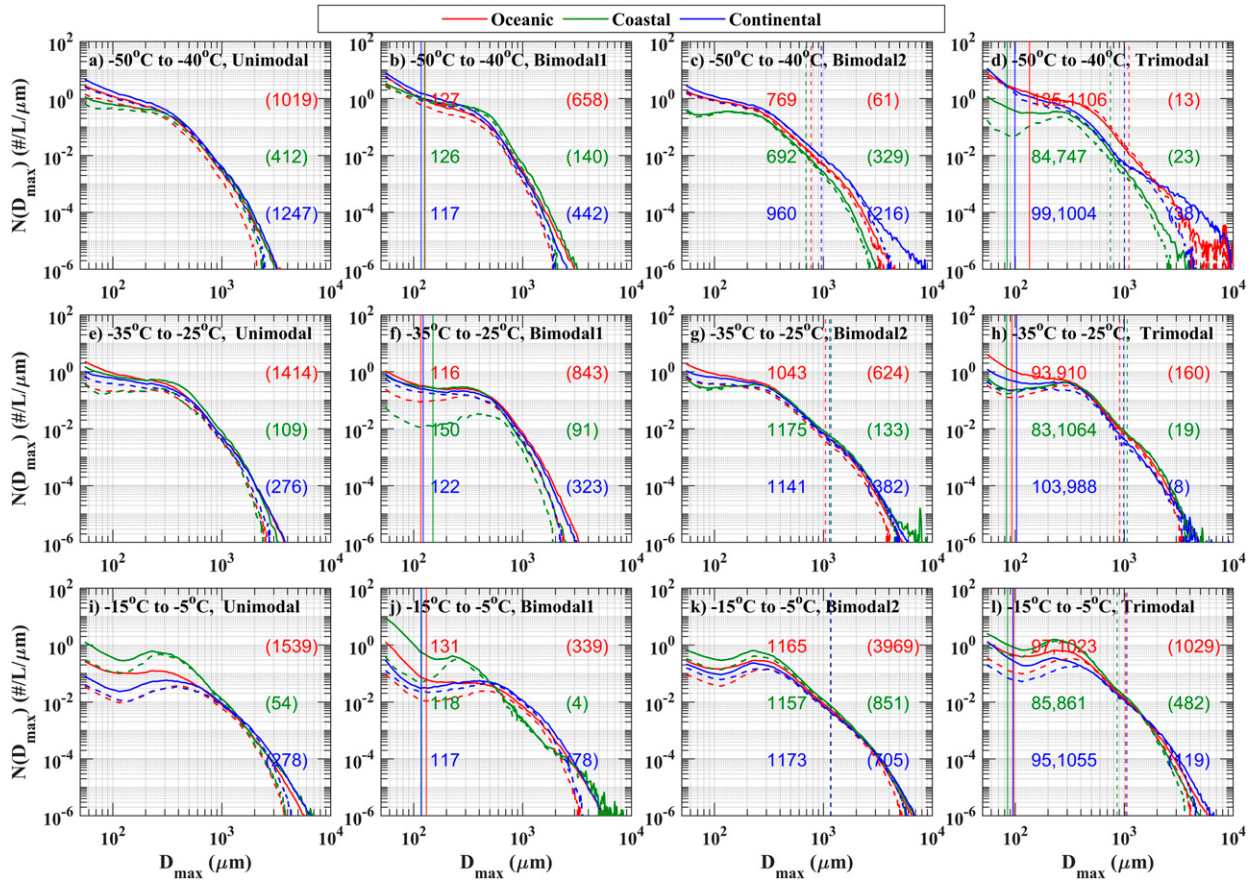


FIG. 18. As in Fig. 6, but segregated according to whether observations are obtained in MCSs over different underlying surface characteristics (land, ocean, or coastal line).

other regions for the same modality and T , similar to the finding of Mascio et al. (2020) showing that $N(D)$ is smallest for stratiform regions, consistent with updrafts regions being the source region of small ice crystals. The mean breakpoints between the two modes for Bimodal1 PSDs are on the average of $100 \pm 30 \mu\text{m}$ with no obvious dependence on T . The mean breakpoints between the two modes for Bimodal2 PSDs are in the range of 992 to $1168 \mu\text{m}$ when $-15^\circ \leq T \leq -5^\circ\text{C}$, but decrease with decreasing T , becoming less than $950 \mu\text{m}$ for $-50^\circ \leq T \leq -40^\circ\text{C}$. There is no obvious dependence of the breakpoints on vertical velocity. For the Trimodal PSDs, the mean breakpoints between the small mode and middle mode are in the range of 85 to $128 \mu\text{m}$, and the mean breakpoints between the middle mode and large mode are in the range of 850 to $1200 \mu\text{m}$, with no strong dependence on either T or vertical motion. The small breakpoints and large breakpoints in Trimodal PSDs are similar to the breakpoints in Bimodal1 PSDs and in Bimodal2 PSDs, respectively, with the same trends for the varying vertical motion.

Figure 13 shows the ellipse projections of the fit parameters in (N_o, μ) phase space for different modalities and vertical velocities as a function of T . The slopes of N_o with λ in the small mode of the Trimodal PSDs are largest, and in the large mode of the Trimodal PSDs are smallest. There are less

obvious changes of the slopes as T changes. However, the ellipses of stratiform regions are larger than those for updrafts and downdrafts. Both N_o and μ can reach larger values in stratiform regions compared to values within updrafts and downdrafts because the IWC is smaller in stratiform regions than in updrafts and downdrafts (Hu et al. 2021).

Figure 14 shows the ellipse projections of the fit parameters in (N_o, λ) phase space for different modalities and vertical velocities as a function of T . For all modalities, λ increases with increasing N_o . Although there is no strong difference in the slopes of N_o and λ on modality for the same T , the ellipses describing stratiform regions tend to be larger than those associated with other vertical motions. The N_o and λ have smaller values in updrafts, consistent with the more likely occurrence of HIWC regions in updrafts and the smaller ellipsoid volumes for the HIWC regions. However, Mascio et al. (2020) found N_o and λ are the largest for updrafts. This difference probably occurs because data were sampled under different meteorological conditions.

Figure 15 shows the projections of fit parameters in (μ, λ) phase space. Similar to the (N_o, λ) and (N_o, μ) phase spaces, the slopes of the long axis of the ellipse in (μ, λ) phase space are positive regardless of modality or T . The ellipses of stratiform regions are usually larger than those for updraft and

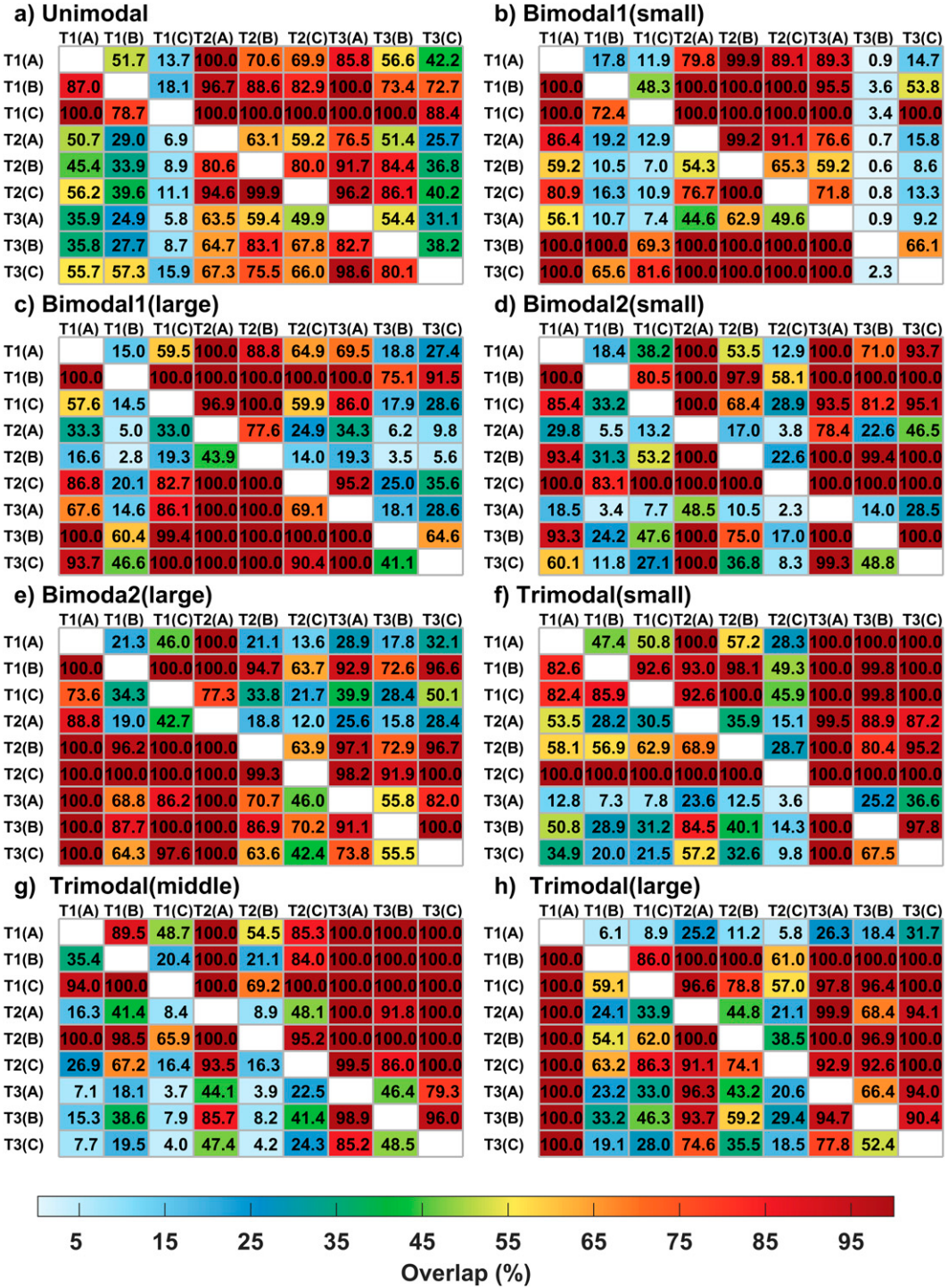


FIG. 19. As in Fig. 10, but for different underlying surface characteristics. A, B, and C represent underlying surface characteristics: oceanic, coastal, and continental MCSs, respectively. T1, T2, and T3 represent $-50^\circ \leq T \leq -40^\circ\text{C}$, $-35^\circ \leq T \leq -25^\circ\text{C}$, and $-15^\circ \leq T \leq -5^\circ\text{C}$, respectively.

downdraft regions for most situations. For Trimodal PSDs, there are obvious differences of slopes between the small mode and middle mode, and less obvious differences between middle mode and large mode.

To quantify how the fit parameters vary with vertical motion, Fig. 16 shows the overlap fraction between the ellipsoid volumes for different T and vertical motions. For the same T , volumes in stratiform regions are usually larger for updrafts

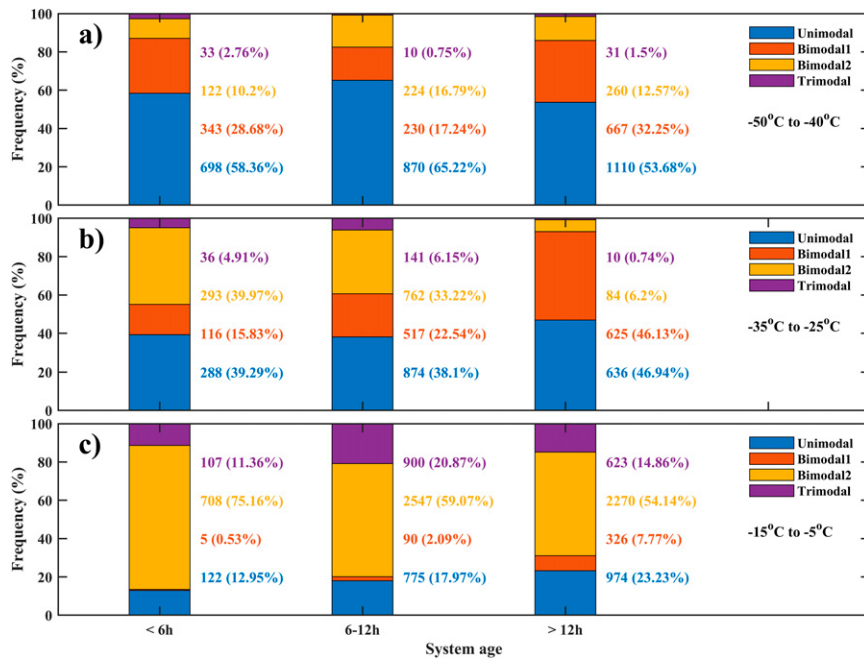


FIG. 20. As in Fig. 5, but segregated according to age of MCS where observations are obtained.

and downdrafts regardless of modality. For example, the percentage overlap is usually less than 70% for stratiform regions when $-15^{\circ} \leq T \leq -5^{\circ}\text{C}$. Further, the volumes in downdrafts are usually larger than for updrafts regions.

c. Surface characteristics

The MCSs were separated into three groups according to whether the convection was observed over the ocean, coastline, or land to compare PSDs as a function of surface characteristics. Figure 17 shows the normalized frequency of the different modalities of these regions as a function of T . The dependence on T seems to be stronger than any dependence on surface characteristics. For example, the frequency of Unimodal PSDs increases and the frequency of multimodal PSDs decreases with decreasing T regardless of surface type. The frequency of multimodal PSDs in coastal MCSs is usually larger than for oceanic or continental convection at the same T , especially for $-15^{\circ} \leq T \leq -5^{\circ}\text{C}$ when multimodal PSDs occur $\sim 96.1\%$ of the time (Fig. 17c). Among the multimodal PSDs, the frequency of Bimodal2 PSDs in coastal MCSs is usually largest reaching $\sim 61.5\%$ of the time when $-15^{\circ} \leq T \leq -5^{\circ}\text{C}$ (Fig. 17c). The frequency of Trimodal PSDs for continental MCSs are smaller than those for oceanic MCSs when $T \leq -35^{\circ}\text{C}$, but an opposite trend is noted when $-50^{\circ} \leq T \leq -40^{\circ}\text{C}$. This is consistent with the findings that higher IWCs are found in oceanic MCSs at lower altitude and higher IWCs in continental MCSs at higher altitude (Hu et al. 2021).

Figure 18 shows the mean (solid line) and median (dashed line) PSDs for different surface characteristics as a function of T . The number of small ice crystals with $D_{\max} < 100 \mu\text{m}$ in continental MCSs is smaller than for the other surface characteristics when $-15^{\circ} \leq T \leq -5^{\circ}\text{C}$, but larger when

$-50^{\circ} \leq T \leq -40^{\circ}\text{C}$, because MCSs over the mainland are usually stronger than over the ocean or coast (e.g., Lucas et al. 1994; Zipser et al. 2006; Matsui et al. 2016), and thus produce more small ice crystals. The mean breakpoints between the two modes for Bimodal1 PSDs are larger than $100 \mu\text{m}$, reaching a maximum of $150 \mu\text{m}$ for Bimodal1 PSDs in Coastal MCSs at $-35^{\circ} \leq T \leq -25^{\circ}\text{C}$. The average breakpoint is $692 \mu\text{m}$ for Bimodal2 PSDs in Coastal MCSs at $-50^{\circ} \leq T \leq -40^{\circ}\text{C}$, smaller than values noted for other T and surface characteristics. The mean small breakpoints ($83\text{--}85 \mu\text{m}$) and large breakpoints ($747\text{--}1064 \mu\text{m}$) for coastal MCSs are usually smaller than those in oceanic MCSs ($93\text{--}135$ and $910\text{--}1106 \mu\text{m}$) and continental MCSs ($95\text{--}103$ and $988\text{--}1055 \mu\text{m}$).

To quantify how the ellipsoids describing the fit parameters vary with surface characteristics, Fig. 19 shows the overlap between the three-dimensional volumes of equally realizable fit parameters for different surface characteristics. Ellipsoids describing continental MCSs have the smallest volumes for Unimodal PSDs at different T , consistent with the parameter ranges being smaller (Figure not shown). The ellipsoid volume overlaps in coastal MCSs at $-50^{\circ} \leq T \leq -40^{\circ}\text{C}$ have the smallest values, and the ellipsoid volume overlaps in oceanic MCSs regions at $-15^{\circ} \leq T \leq -5^{\circ}\text{C}$ have the smallest values for most conditions. And the ellipsoids for coastal MCSs are usually smaller than for oceanic MCSs for different modality PSDs.

d. System age

To compare PSDs for different system ages, the MCS age was sorted into three groups (<6 , $6\text{--}12$, >12 h). Figure 20 shows the normalized frequency of the different modalities for MCSs with different ages as a function of T . There is a

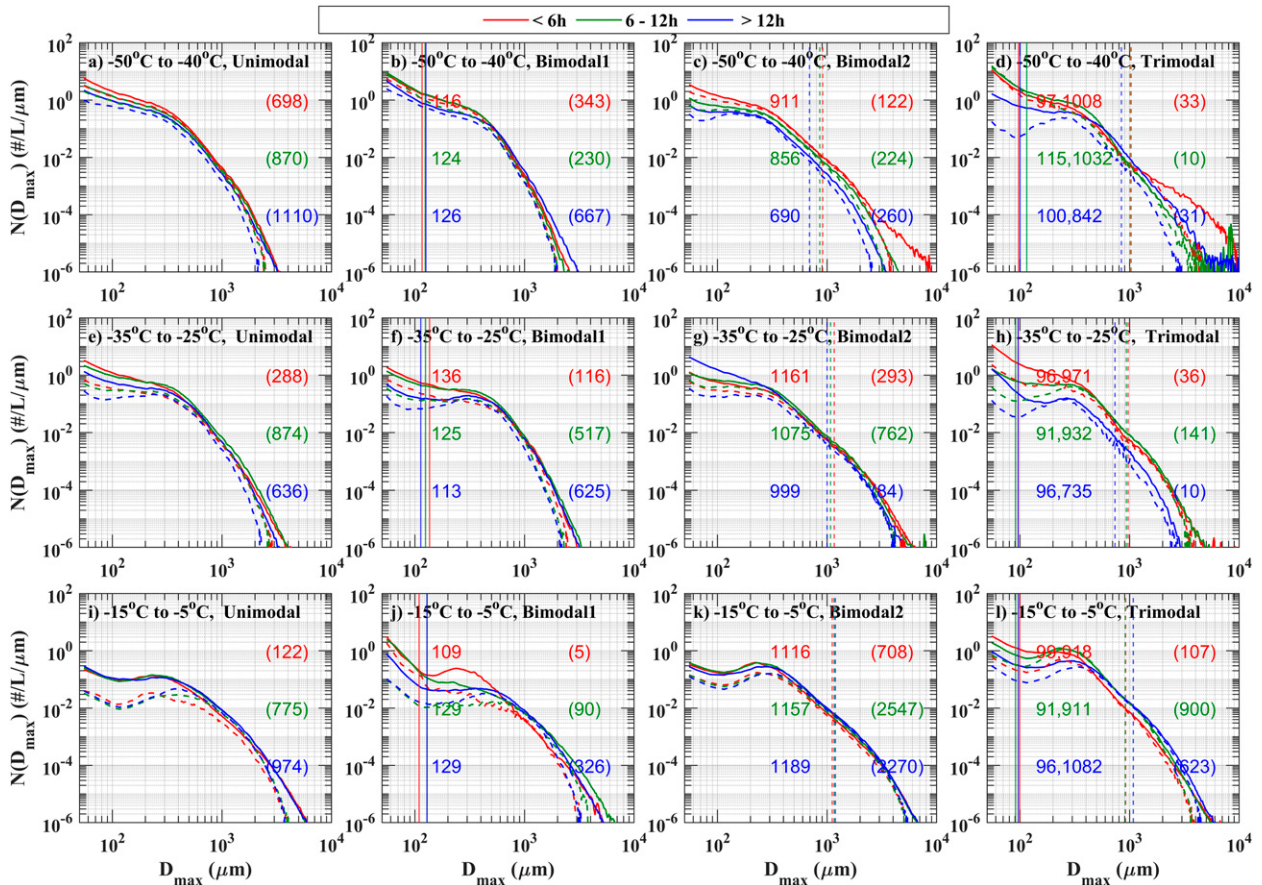


FIG. 21. As in Fig. 6, but segregated according to age of system where observations are obtained.

stronger dependence of the modality with T than on the system age. Nevertheless, the frequency of Unimodal PSDs increases with system age for $T \geq -35^\circ\text{C}$, while the frequency of Trimodal PSDs is the largest for system age between 6 and 12 h (Figs. 20b,c). This is consistent with the 6–12 h stage representing the developing or mature stage after ice has started being injected into the anvil (Leary and Houze 1980), with many ice crystals being created and growing by aggregation (Hu et al. 2021). For the multimodal PSDs, the frequency of Bimodal1 PSDs in MCSs age > 12 h is largest for each T , reaching to $\sim 46.1\%$ when $-35^\circ \leq T \leq -25^\circ\text{C}$ (Fig. 20b). On the other hand, the frequency of Trimodal PSDs in MCS ages > 12 h is usually the smallest for $T \leq -25^\circ\text{C}$, due to the IWC in the >12 h age is the smallest, consistent with sublimation and a weakening and dissipation of MCSs not being conducive to the generation and growth of ice particles (Hu et al. 2021).

Figure 21 shows the mean (solid line) and median (dashed line) PSDs as a function of MCS age and T . For most conditions, the $N(D_{\max})$ for younger system ages are usually larger than those in older MCSs for $D_{\max} < 200 \mu\text{m}$ because more ice crystals are produced in the developing and mature stages. The differences between Trimodal PSDs for different MCS ages are more obvious than for other modality PSDs at all T .

Breakpoints between the two modes in Bimodal2 PSDs increase with increasing T for all MCS ages. The breakpoints in Bimodal2 and the breakpoints between the second and third mode in Trimodal PSDs are the smallest for MCS ages > 12 h when $T \leq -25^\circ\text{C}$.

To quantify the difference between the overlapping ellipsoids of equally plausible solutions for different T and MCS ages, Fig. 22 shows the overlap between the three-dimensional volumes of equally realizable fit parameters for different MCS ages and T for the four modalities. The most apparent feature is that for different modality PSDs, the ellipsoid volumes for MCSs with ages < 6 h at $-50^\circ \leq T \leq -40^\circ\text{C}$ are largest. For example, for the small mode of Bimodal2 PSDs, the overlaps are mostly less than 80% when MCS ages are in < 6 h at $-50^\circ \leq T \leq -40^\circ\text{C}$, while more than 80% are found in other ellipsoids (Fig. 22d).

e. Distance away from the convective core

To compare the PSDs with distance away from the convective core (L), PSDs were divided into four groups ($L \leq 50 \text{ km}$, $50 < L \leq 100 \text{ km}$, $100 < L \leq 200 \text{ km}$, $L > 200 \text{ km}$). Figure 23 shows the normalized frequency of the four different modalities as a function of L and T . The dependence on T is stronger than the dependence on L . However, there are still some trends

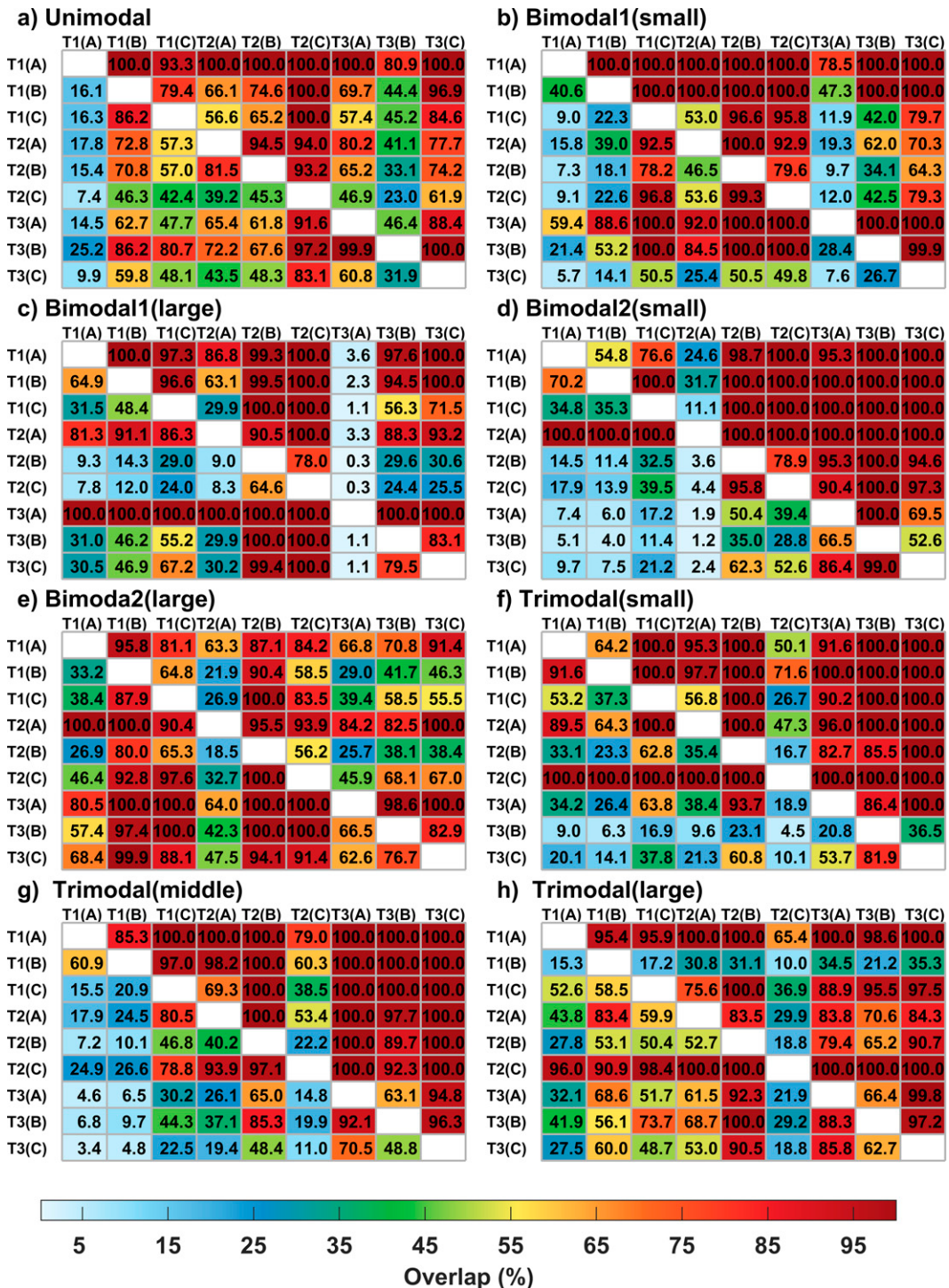


FIG. 22. As in Fig. 10, but segregated according to MCS age. A, B, and C represents MCS ages within <6, 6–12, and >12 h, respectively. T1, T2, and T3 represent $-50^\circ \leq T \leq -40^\circ\text{C}$, $-35^\circ \leq T \leq -25^\circ\text{C}$, and $-15^\circ \leq T \leq -5^\circ\text{C}$, respectively.

with L . The frequency of Trimodal PSDs decreases slowly with increasing L when $-15^\circ \leq T \leq -5^\circ\text{C}$, and the frequency of Bimodal2 PSDs is larger for regions away from the convective core when $T \leq -25^\circ\text{C}$, while the opposite trends are realized

for Bimodal1 PSDs (Figs. 23a,b) as the frequency of Bimodal1 PSDs is smallest for these regions at the same T . In summary, changes in the frequency of PSD modality with L is less obvious, probably due to horizontal wind transport. T is still

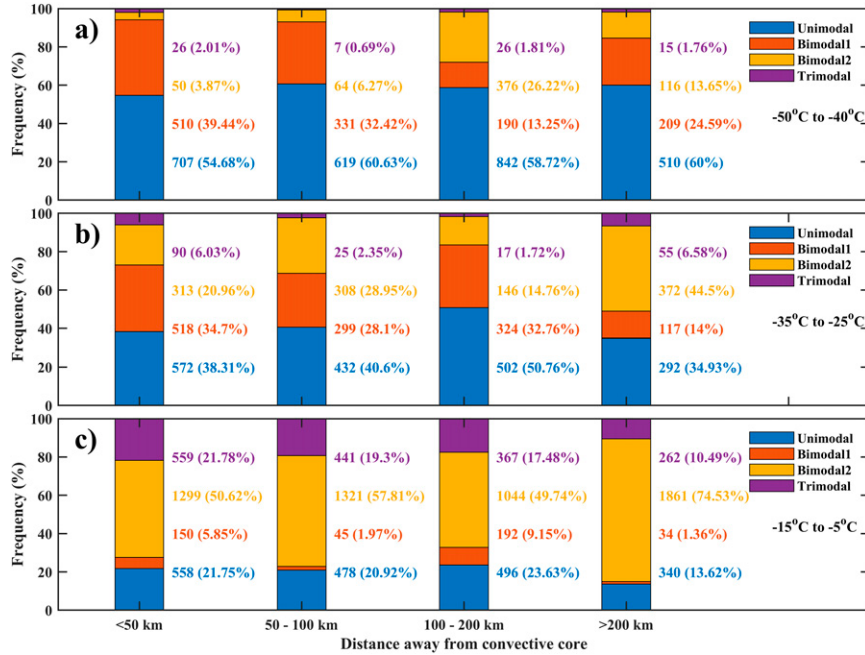


FIG. 23. As in Fig. 5, but segregated according to distance away from convective core where observations are obtained.

the important factor, the frequency of Unimodal PSDs increases, and multimodal PSDs decrease with decreasing T for different L .

Figure 24 shows the mean (solid line) and median (dashed line) PSDs as a function of T and L . There are less obvious differences for Unimodal, Bimodal1 and Bimodal2 PSDs between different L at the same T . Breakpoints between the two modes in Bimodal1 PSDs show less obvious changes with increasing T , the breakpoints between the two modes in Bimodal2 PSDs within different L increase with increasing T . For example, the mean breakpoint is 757 μm for Bimodal2 PSDs with $L > 200 \text{ km}$ when $-50^\circ \leq T \leq -40^\circ\text{C}$, while it increases to 1194 μm when $-15^\circ \leq T \leq -5^\circ\text{C}$. Less obvious differences exist between the breakpoints within different L for the same modality PSDs and same T .

To quantify the difference between the ellipsoids of equally plausible solutions for different L , Fig. 25 shows the overlap between the three-dimensional volumes of equally realizable fit parameters for different L and T for the four modalities. Less obvious regular trends between different L at the same T , consistent with the finding of Mascio et al. (2020), due to the distributions of IWCs with L are different at different T (Korolev et al. 2018; Hu et al. 2021).

5. Conclusions

To quantitatively describe the difference of particle size distributions (PSDs) as a function of environmental conditions, data obtained during the second HAIC-HIWC flight campaign conducted from 9 to 29 May 2015 out of Cayenne, French Guiana, were analyzed. Data were separated according

to temperature (T ; $-15^\circ \leq T \leq -5^\circ\text{C}$; $-35^\circ \leq T \leq -25^\circ\text{C}$; $-50^\circ \leq T \leq -40^\circ\text{C}$), vertical velocity (updrafts, downdrafts, and stratiform cloud regions), surface conditions (oceanic, coastal and continental), MCS age (<6 , $6-12$, >12 h), and distance away from the convective core ($L \leq 50 \text{ km}$; $50 < L \leq 100 \text{ km}$; $100 < L \leq 200 \text{ km}$; $L > 200 \text{ km}$). The difference of PSDs between HIWC regions was also contrasted against those obtained in regions without HIWCs. The principal findings of this study are as follows:

- 1) HIWC regions ($\text{IWC} \geq 1.5 \text{ g m}^{-3}$) with small MMD ($<500 \mu\text{m}$) are full of small columns and irregular ice crystals at $-15^\circ \leq T \leq -5^\circ\text{C}$, consistent with negative correlation between IWC and MMD within the HIWC regions. The distributions of ice crystals shapes are different for different IWC regions.
- 2) Data from the Cayenne campaign were used to determine how many modes were required to represent the PSD using a new methodology that automatically determines the number of modes and gamma fit parameters for each mode in a multimodal PSD. Four kinds of modalities of PSDs were found by this method.
- 3) The T has the largest effect on PSD shape, and hence on the number of modes and the fit parameters describing each mode of the PSDs. The frequency of multimodal PSDs increases and the frequency of unimodal PSD decreases with increasing T , consistent with heterogeneous nucleation in the presence of particles sedimenting from above (Zhao et al. 2010) and the aggregation process.
- 4) The number and location of the modes in a PSD (modalities) are also related to IWC. The frequency of multimodal

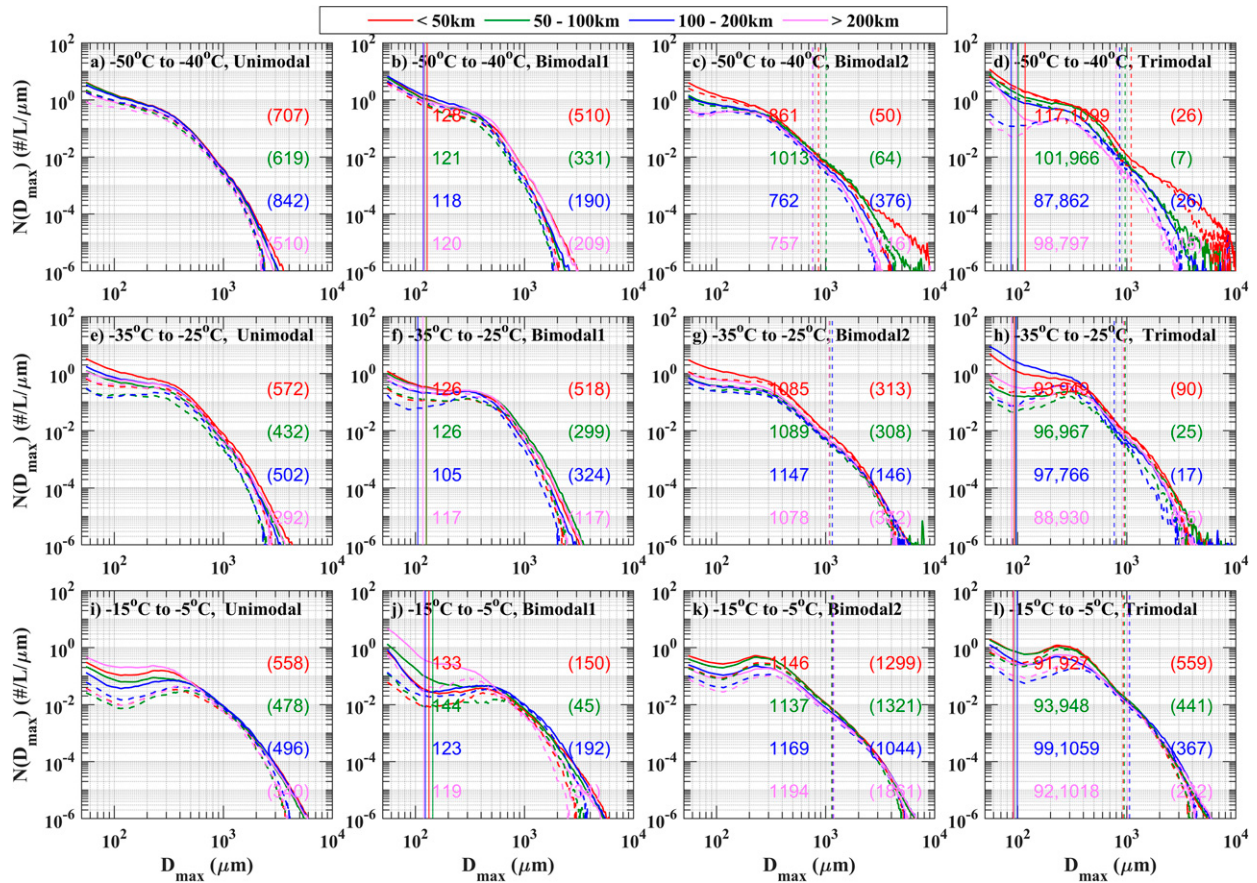


FIG. 24. As Fig. 6, but segregated according to distance away from convective core where observations are obtained.

PSDs increases with IWC and the frequency of unimodal PSDs decreases with IWC. There was no strong trend in how frequency distributions of IWC and MMD varied with the modality of the PSD.

- 5) The frequency of Unimodal and multimodal PSDs depends on vertical velocity (w), consistent with the impact of w on IWC. The largest frequency of Trimodal PSDs occurs in updrafts. There is some dependence on the distributions of modality on other environmental conditions (e.g., underlying surface characteristics, MCS age, the distance away from the convective core), which is not as strong as the dependence on T and can be related to the dependence of IWC on environmental conditions.
- 6) The breakpoints between the two modes in the Bimodal1 PSDs occur at a D_{\max} of $100 \pm 20 \mu\text{m}$ with no strong dependence on T . Breakpoints between the two modes in the Bimodal2 PSDs are located at a D_{\max} of around $1000 \pm 300 \mu\text{m}$ and increase with T . The breakpoints that exist in Trimodal PSDs are similar to the breakpoints in the two types of bimodal PSDs.
- 7) The three fit parameters ($N_o-\lambda-\mu$) characterizing the gamma distribution of each mode are interdependent. For the same λ , N_o , and μ are larger in the large modes with larger D_{\max} compared to the small modes, consistent with particles with smaller D_{\max} consisting of recently nucleated particles

that have not significantly grown by vapor deposition, and particles with larger D_{\max} having undergone sorting by sedimentation and deposition (Jackson et al. 2015).

- 8) The μ decreases with IWC for the same N_o , and the ranges of λ and N_o both narrow with increasing IWC. This is consistent with more smaller ice crystals being found in the high IWC regions.
- 9) The HIWC regions have the smallest ellipsoids, indicating that the parameters (N_o , μ , and λ) are constrained for HIWC regions compared to other regions and also meaning the least uncertainty in parameters for such conditions.

The findings presented here apply only to data collected in the vicinity of Cayenne, French Guiana, during HAIC-HIWC. The techniques developed here can be applied to data collected elsewhere to determine the robustness of the findings. Future studies should seek to obtain data on more diverse geographic locations, and implement parameterizations of PSDs developed here in ensemble or stochastic simulations that can be used to test processes responsible to occurrence of large numbers of small ice crystals. Model simulations using parameterizations of PSDs with three modes should be conducted to see if they improve upon simulations conducted using one-mode parameterizations as such simulations should better represent processes without the additional computational

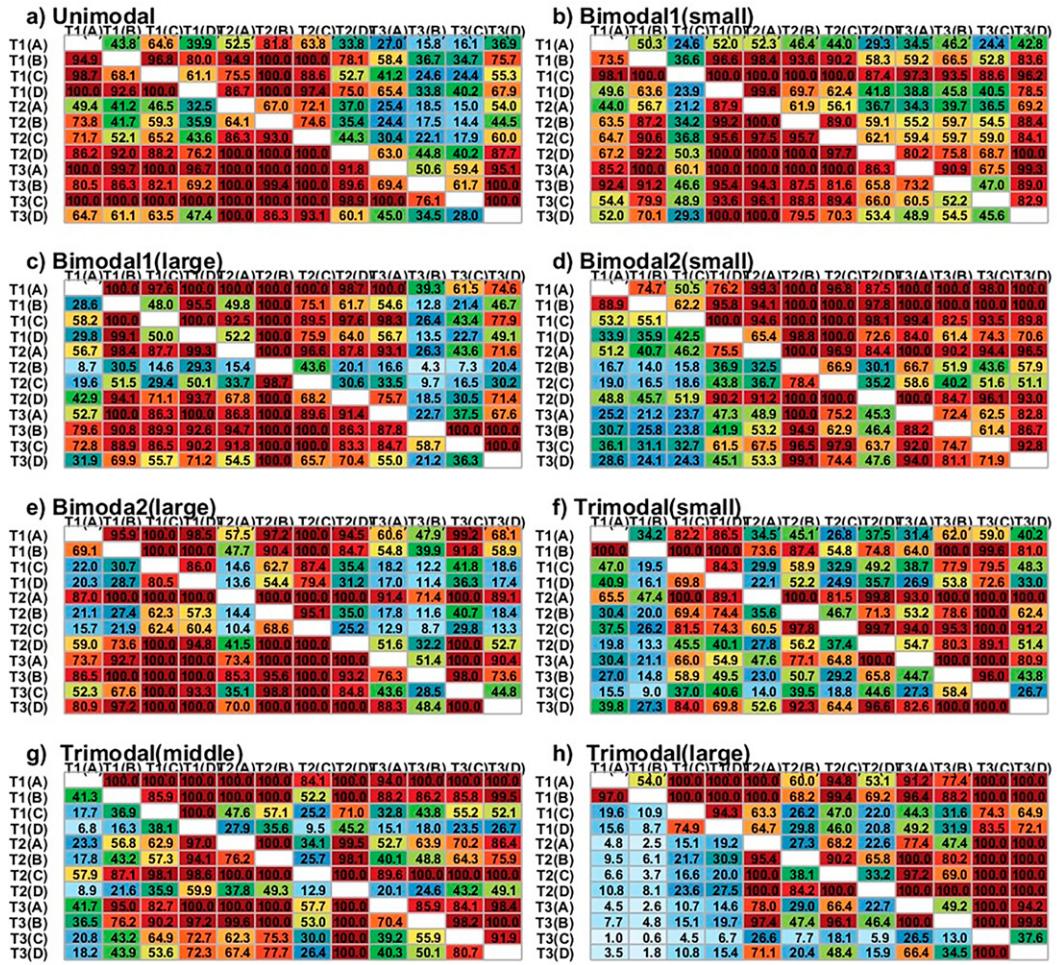


FIG. 25. As in Fig. 10, but segregated according to distance away from convective core where observations are obtained. A, B, C, and D represent four regions within $L \leq 50$ km, $50 < L \leq 100$ km, $100 < L \leq 200$ km, and $L > 200$ km, respectively. T1, T2, and T3 represent $-50^\circ \leq T \leq -40^\circ\text{C}$, $-35^\circ \leq T \leq -25^\circ\text{C}$, and $-15^\circ \leq T \leq -5^\circ\text{C}$, respectively.

expense of a bin-resolved scheme. Future work also needs to better determine reasons for the variability of surfaces characterizing the PSDs, including examining whether the surfaces and the modality vary with concentrations of cloud condensation nuclei and ice nucleating particles. In addition, care should be taken to isolate the differences in the PSD surfaces that are caused by variations in meteorological and aerosol conditions, as opposed to differences that arise due to differences in probes used to collect the data and algorithms used to process the data.

Acknowledgments. This work was supported by the National Science Foundation (Awards 1213311 and 1842094). Observation data are provided through NCAR/EOL under the sponsorship of the National Science Foundation (<https://data.eol.ucar.edu/>). NCAR is sponsored by the National

Science Foundation. Major North American funding for flight campaigns was provided by the FAA William Hughes Technical Center and Aviation Weather Research Program, the NASA Aeronautics Research Mission Directorate Aviation Safety Program, the Boeing Co., Environment and Climate Change Canada, the National Research Council of Canada, and Transport Canada. Major European campaign and research funding was provided from (i) the European Commission Seventh Framework Programme in research, technological development, and demonstration under Grant ACP2-GA-2012-314314, (ii) the European Safety Agency (EASA) Research Programme under Service Contract EASA.2013.FC27. Further funding was provided by the Ice Crystal Consortium. Some of the computing for this project was performed at the University of Oklahoma (OU) Supercomputing Center for Education and

Research (OSCER). The discussions of HIWC conditions and aircraft measurements with Walter Strapp are greatly appreciated. The first author is also supported by the China Scholarship Council (CSC). The authors are also grateful to all of whom provided helpful comments and suggestions that improved the manuscript.

Data availability statement. Observation data are available at https://data.eol.ucar.edu/master_lists/generated/haic-hiwc_2015. The GOES-13 data are available over the domain of 0°–10°N, 45°–60°W where the aircraft flew during the Cayenne campaign (<https://doi.org/10.5065/D6NC5ZX6>).

REFERENCES

- Ackerman, T. P., K. N. Liou, F. P. Valero, and L. Pfister, 1988: Heating rates in tropical anvils. *J. Atmos. Sci.*, **45**, 1606–1623, [https://doi.org/10.1175/1520-0469\(1988\)045,1606:HRITA.2.0.CO;2](https://doi.org/10.1175/1520-0469(1988)045,1606:HRITA.2.0.CO;2).
- Bailey, M. P., and J. Hallett, 2009: A comprehensive habit diagram for atmospheric ice crystals: Confirmation from the laboratory, AIRS II, and other field studies. *J. Atmos. Sci.*, **66**, 2888–2899, <https://doi.org/10.1175/2009JAS2883.1>.
- Baumgardner, D., and Coauthors, 2017: Cloud ice properties: In situ measurement challenges. *Ice Formation and Evolution in Clouds and Precipitation: Measurement and Modeling Challenges*, Meteor. Monogr., No. 58, Amer. Meteor. Soc., <https://doi.org/10.1175/AMSMONOGRAPHS-D-16-0011.1>.
- Brechner, P., 2021: Ice crystal size distributions in tropical mesoscale convective systems in the vicinity of Darwin, Australia: Results from the HAIC/HIWC campaign. M.S. thesis, School of Meteorology, University of Oklahoma, 57 pp., <https://hdl.handle.net/11244/332327>.
- Brown, P. R., and P. N. Francis, 1995: Improved measurements of the ice water content in cirrus using a total-water probe. *J. Atmos. Oceanic Technol.*, **12**, 410–414, [https://doi.org/10.1175/1520-0426\(1995\)012<0410:IMOTIW>2.0.CO;2](https://doi.org/10.1175/1520-0426(1995)012<0410:IMOTIW>2.0.CO;2).
- Bryan, G. H., and H. Morrison, 2012: Sensitivity of a simulated squall line to horizontal resolution and parameterization of microphysics. *Mon. Wea. Rev.*, **140**, 202–225, <https://doi.org/10.1175/MWR-D-11-00046.1>.
- Chandrasekar, V., and V. N. Bringi, 1987: Simulation of radar reflectivity and surface measurements of rainfall. *J. Atmos. Oceanic Technol.*, **4**, 464–478, [https://doi.org/10.1175/1520-0426\(1987\)004,0464:SORRAS.2.0.CO;2](https://doi.org/10.1175/1520-0426(1987)004,0464:SORRAS.2.0.CO;2).
- Chen, C. H., C. L. Su, J. H. Chen, and Y. H. Chu, 2020: Vertical wind effect on slope and shape parameters of gamma drop size distribution. *J. Atmos. Oceanic Technol.*, **37**, 243–262, <https://doi.org/10.1175/JTECH-D-18-0026.1>.
- Chen, S., and W. Cotton, 1988: The sensitivity of a simulated extratropical mesoscale convective system to longwave radiation and ice-phase microphysics. *J. Atmos. Sci.*, **45**, 3897–3910, [https://doi.org/10.1175/1520-0469\(1988\)045<3897:TSOASE>2.0.CO;2](https://doi.org/10.1175/1520-0469(1988)045<3897:TSOASE>2.0.CO;2).
- Clark, A. J., and Coauthors, 2012: An overview of the 2010 Hazardous Weather Testbed Experimental Forecast Program Spring Experiment. *Bull. Amer. Meteor. Soc.*, **93**, 55–74, <https://doi.org/10.1175/BAMS-D-11-00040.1>.
- Del Genio, A. D., and W. Kovari, 2002: Climatic properties of tropical precipitating convection under varying environmental conditions. *J. Climate*, **15**, 2597–2615, [https://doi.org/10.1175/1520-0442\(2002\)015<2597:CPOTPC>2.0.CO;2](https://doi.org/10.1175/1520-0442(2002)015<2597:CPOTPC>2.0.CO;2).
- Dezitter, F., A. Grandin, J. L. Brenguier, F. Hervy, H. Schlager, P. Villedieu, and G. Zalamansky, 2013: HAIC (High Altitude Ice Crystals). *Proc. Fifth AIAA Atmospheric and Space Environments Conf.*, AIAA-2013-2674, San Diego, CA, American Institute of Aeronautics and Astronautics, <http://arc.aiaa.org/doi/abs/10.2514/6.2013-2674>.
- Ding, S., G. M. McFarquhar, S. W. Nesbitt, R. J. Chase, M. R. Poellot, and H. Wang, 2020: Dependence of mass-dimensional relationships on median mass diameter. *Atmosphere*, **11**, 756, <https://doi.org/10.3390/atmos11070756>.
- DMT, 2009: Single particle imaging. Data analysis user's guide, DOC-0223, Rev. A, 34 pp.
- Field, P. R., R. J. Hogan, P. R. A. Brown, A. J. Illingworth, T. W. Choularton, and R. J. Cotton, 2005: Parametrization of ice-particle size distributions for mid-latitude stratiform cloud. *Quart. J. Roy. Meteor. Soc.*, **131**, 1997–2017, <https://doi.org/10.1256/qj.04.134>.
- Finlon, J. A., G. M. McFarquhar, S. W. Nesbitt, R. M. Rauber, H. Morrison, W. Wu, and P. Zhang, 2019: A novel approach for characterizing the variability in mass-dimension relationships: Results from MC3E. *Atmos. Chem. Phys.*, **19**, 3621–3643, <https://doi.org/10.5194/acp-19-3621-2019>.
- Fontaine, E., and Coauthors, 2017: Evaluation of radar reflectivity factor simulations of ice crystal populations from in situ observations for the retrieval of condensed water content in tropical mesoscale convective systems. *Atmos. Meas. Tech.*, **10**, 2239–2252, <https://doi.org/10.5194/amt-10-2239-2017>.
- Fu, Q., 1996: An accurate parameterization of the solar radiative properties of cirrus clouds for climate models. *J. Climate*, **9**, 2058–2082, [https://doi.org/10.1175/1520-0442\(1996\)009<2058:AAPOTS>2.0.CO;2](https://doi.org/10.1175/1520-0442(1996)009<2058:AAPOTS>2.0.CO;2).
- , S. K. Krueger, and K. N. Liou, 1995: Interactions of radiation and convection in simulated tropical cloud clusters. *J. Atmos. Sci.*, **52**, 1310–1328, [https://doi.org/10.1175/1520-0469\(1995\)052<1310:IORACI>2.0.CO;2](https://doi.org/10.1175/1520-0469(1995)052<1310:IORACI>2.0.CO;2).
- Gilmore, M. S., J. M. Straka, and E. N. Rasmussen, 2004: Precipitation uncertainty due to variations in precipitation particle parameters within a simple microphysics scheme. *Mon. Wea. Rev.*, **132**, 2610–2627, <https://doi.org/10.1175/MWR2810.1>.
- Gu, Y., K. N. Liou, S. C. Ou, and R. Fovell, 2011: Cirrus cloud simulations using WRF with improved radiation parameterization and increased vertical resolution. *J. Geophys. Res.*, **116**, D06119, <https://doi.org/10.1029/2010JD014574>.
- Gunn, K. L. S., and J. S. Marshall, 1958: The distribution with size of aggregate snowflakes. *J. Meteor.*, **15**, 452–461, [https://doi.org/10.1175/1520-0469\(1958\)015<0452:TDWSOA>2.0.CO;2](https://doi.org/10.1175/1520-0469(1958)015<0452:TDWSOA>2.0.CO;2).
- Haddad, Z. S., S. L. Durden, and E. Im, 1996: Parameterizing the raindrop size distribution. *J. Appl. Meteor.*, **35**, 3–13, [https://doi.org/10.1175/1520-0450\(1996\)035<0003:PTRSD>2.0.CO;2](https://doi.org/10.1175/1520-0450(1996)035<0003:PTRSD>2.0.CO;2).
- Handwerker, J., and W. Straub, 2011: Optimal determination of parameters for gamma-type drop size distributions based on moments. *J. Atmos. Oceanic Technol.*, **28**, 513–529, <https://doi.org/10.1175/2010JTECHA1474.1>.
- Heymsfield, A. J., and G. M. McFarquhar, 2002: Mid-latitude and tropical cirrus: Microphysical properties. *Cirrus*, D. Lynch et al., Eds., Oxford University Press, 78–101.
- , A. Bansemer, G. Heymsfield, and A. O. Fierro, 2009: Microphysics of maritime tropical convective updrafts at temperatures from –20° to –60°. *J. Atmos. Sci.*, **66**, 3530–3562, <https://doi.org/10.1175/2009JAS3107.1>.

- , C. Schmitt, and A. Bansemer, 2013: Ice cloud particle size distributions and pressure-dependent terminal velocities from in situ observations at temperatures from 0° to -86°C. *J. Atmos. Sci.*, **70**, 4123–4154, <https://doi.org/10.1175/JAS-D-12-0124.1>.
- Hu, Y., and Coauthors, 2021: Dependence of ice microphysical properties on environmental parameters: Results from HAIC-HIWC Cayenne field campaign. *J. Atmos. Sci.*, **78**, 2957–2981, <https://doi.org/10.1175/JAS-D-21-0015.1>.
- Huang, Y., Y. Wang, L. Xue, X. Wei, L. Zhang, and H. Li, 2020: Comparison of three microphysics parameterization schemes in the WRF model for an extreme rainfall event in the coastal metropolitan city of Guangzhou, China. *Atmos. Res.*, **240**, 10493, <https://doi.org/10.1016/j.atmosres.2020.104939>.
- , and Coauthors, 2021: Microphysical processes producing high ice water contents (HIWCs) in tropical convective clouds during the HAIC-HIWC field campaign: Evaluation of simulations using bulk microphysical schemes. *Atmos. Chem. Phys.*, **21**, 6919–6944, <https://doi.org/10.5194/acp-21-6919-2021>.
- Jackson, R. C., G. M. McFarquhar, J. Stith, M. Beals, R. A. Shaw, J. Jensen, J. Fugal, and A. Korolev, 2014: An assessment of the impact of antishattering tips and artifact removal techniques on cloud ice size distributions measured by the 2D cloud probe. *J. Atmos. Oceanic Technol.*, **31**, 2567–2590, <https://doi.org/10.1175/JTECH-D-14-00018.1>.
- , —, A. M. Fridlind, and R. Atlas, 2015: The dependence of cirrus gamma size distributions expressed as volumes in N0- λ - μ phase space and bulk cloud properties on environmental conditions: Results from the Small Ice Particles in Cirrus Experiment (SPARTICUS). *J. Geophys. Res. Atmos.*, **120**, 10351–10377, <https://doi.org/10.1002/2015JD023492>.
- Jakob, C., and S. A. Klein, 1999: The role of vertically varying cloud fraction in the parametrization of microphysical processes in the ECMWF model. *Quart. J. Roy. Meteor. Soc.*, **125**, 941–965, <https://doi.org/10.1002/qj.49712555510>.
- Jensen, E. J., and Coauthors, 2009: On the importance of small ice crystals in tropical anvil cirrus. *Atmos. Chem. Phys.*, **9**, 5519–5537, <https://doi.org/10.5194/acp-9-5519-2009>.
- Jorgensen, D. P., E. J. Zipser, and M. A. LeMone, 1985: Vertical motions in intense hurricanes. *J. Atmos. Sci.*, **42**, 839–856, [https://doi.org/10.1175/1520-0469\(1985\)042<0839:VMIH>2.0.CO;2](https://doi.org/10.1175/1520-0469(1985)042<0839:VMIH>2.0.CO;2).
- Korolev, A. V., and G. A. Isaac, 2006: Relative humidity in liquid, mixed-phase, and ice clouds. *J. Atmos. Sci.*, **63**, 2865–2880, <https://doi.org/10.1175/JAS3784.1>.
- , and P. Field, 2015: Assessment of the performance of the inter-arrival time algorithm to identify ice shattering artifacts in cloud particle probe measurements. *Atmos. Meas. Tech.*, **8**, 761–777, <https://doi.org/10.5194/amt-8-761-2015>.
- , E. F. Emery, J. W. Strapp, S. G. Cober, G. A. Isaac, M. Wasey, and D. Marcotte, 2011: Small ice particles in tropospheric clouds: Fact or artifact? Airborne icing instrumentation evaluation experiment. *Bull. Amer. Meteor. Soc.*, **92**, 967–973, <https://doi.org/10.1175/2010BAMS3141.1>.
- , —, —, —, and —, 2013: Quantification of the effects of shattering on airborne ice particle measurements. *J. Atmos. Oceanic Technol.*, **30**, 2527–2553, <https://doi.org/10.1175/JTECH-D-13-00115.1>.
- , A. Shashkov, and H. Barker, 2014: Calibrations and performance of the airborne cloud extinction probe. *J. Atmos. Oceanic Technol.*, **31**, 326–345, <https://doi.org/10.1175/JTECH-D-13-00020.1>.
- , I. Heckman, and M. Wolde, 2018: Observation of phase composition and humidity in oceanic mesoscale convective systems. *15th Conf. on Cloud Physics*, 236, Vancouver, BC, Canada, Amer. Meteor. Soc., https://ams.confex.com/ams/15CLOUD15_ATRAD/webprogram/Paper347111.html.
- Lance, S., C. A. Brock, D. Rogers, and J. A. Gordon, 2010: Water droplet calibration of the Cloud Droplet Probe (CDP) and in-flight performance in liquid, ice and mixed-phase clouds during ARCPAC. *Atmos. Meas. Tech.*, **3**, 1683–1706, <https://doi.org/10.5194/amt-3-1683-2010>.
- Lawson, R. P., E. Jensen, D. L. Mitchell, B. Barker, Q. Mo, and B. Pilson, 2010: Microphysical and radiative properties of tropical clouds investigated in TC4 and NAMMA. *J. Geophys. Res.*, **115**, D00J08, <https://doi.org/10.1029/2009JD013017>.
- Leary, C. A., and R. A. Houze Jr., 1980: The contribution of mesoscale motions to the mass and heat fluxes of an intense tropical convective system. *J. Atmos. Sci.*, **37**, 784–796, [https://doi.org/10.1175/1520-0469\(1980\)037<0784:TCOMMT>2.0.CO;2](https://doi.org/10.1175/1520-0469(1980)037<0784:TCOMMT>2.0.CO;2).
- Leroy, D., and Coauthors, 2016a: HAIC/HIWC field campaigns—Specific findings on ice crystals characteristics in high ice water content cloud regions, *8th AIAA Atmospheric and Space Environments Conf.*, AIAA 2016-4056, Washington, DC, AIAA, <https://doi.org/10.2514/6.2016-4056>.
- , E. Fontaine, A. Schwarzenboeck, and J. W. Strapp, 2016b: Ice crystal sizes in high ice water content clouds. Part I: On the computation of median mass diameters from in situ measurements. *J. Atmos. Oceanic Technol.*, **33**, 2461–2476, <https://doi.org/10.1175/JTECH-D-15-0151.1>.
- , and Coauthors, 2017: Ice crystal sizes in high ice water content clouds. Part 2: Median mass diameter statistics in tropical convection observed during the HAIC/HIWC project. *J. Atmos. Oceanic Technol.*, **34**, 117–136, <https://doi.org/10.1175/JTECH-D-15-0246.1>.
- Li, X., and Z. Pu, 2008: Sensitivity of numerical simulation of early rapid intensification of Hurricane Emily (2005) to cloud microphysical and planetary boundary layer parameterizations. *Mon. Wea. Rev.*, **136**, 4819–4838, <https://doi.org/10.1175/2008MWR2366.1>.
- Lin, Y., and B. A. Colle, 2011: A new bulk microphysical scheme that includes riming intensity and temperature-dependent ice characteristics. *Mon. Wea. Rev.*, **139**, 1013–1035, <https://doi.org/10.1175/2010MWR3293.1>.
- Locatelli, J. D., and P. V. Hobbs, 1974: Fall speeds and masses of solid precipitation particles. *J. Geophys. Res.*, **79**, 2185–2197, <https://doi.org/10.1029/JC079i015p02185>.
- Lucas, C., E. J. Zipser, and M. A. LeMone, 1994: Vertical velocity in oceanic convection off tropical Australia. *J. Atmos. Sci.*, **51**, 3183–3193, [https://doi.org/10.1175/1520-0469\(1994\)051<3183:VVIODO>2.0.CO;2](https://doi.org/10.1175/1520-0469(1994)051<3183:VVIODO>2.0.CO;2).
- Machado, L. A. T., and W. B. Rossow, 1993: Structural characteristics and radiative properties of tropical cloud clusters. *Mon. Wea. Rev.*, **121**, 3234–3260, [https://doi.org/10.1175/1520-0493\(1993\)121<3234:SCARPO>2.0.CO;2](https://doi.org/10.1175/1520-0493(1993)121<3234:SCARPO>2.0.CO;2).
- Mascio, J., G. M. McFarquhar, T. L. Hsieh, M. Freer, A. Dooley, and A. J. Heymsfield, 2020: The use of gamma distributions to quantify the dependence of cloud particle size distributions in hurricanes on cloud and environmental conditions. *Quart. J. Roy. Meteor. Soc.*, **146**, 2116–2137, <https://doi.org/10.1002/qj.3782>.
- Matsui, T., J. Chern, W. Tao, S. Lang, M. Satoh, T. Hashino, and T. Kubota, 2016: On the land–ocean contrast of tropical convection and microphysics statistics derived from TRMM satellite signals and global storm-resolving models. *J. Hydrometeor.*, **17**, 1425–1445, <https://doi.org/10.1175/JHM-D-15-0111.1>.

- Mazin, I. P., A. V. Korolev, A. Heymsfield, G. A. Isaac, and S. G. Cober, 2001: Thermodynamics of icing cylinder for measurements of liquid water content in supercooled clouds. *J. Atmos. Oceanic Technol.*, **18**, 543–558, [https://doi.org/10.1175/1520-0426\(2001\)018<0543:TOICFM>2.0.CO;2](https://doi.org/10.1175/1520-0426(2001)018<0543:TOICFM>2.0.CO;2).
- McCumber, M., W. K. Tao, J. Simpson, R. Penc, and S. T. Soong, 1991: Comparison of ice-phase microphysical parameterization schemes using numerical simulations of tropical convection. *J. Appl. Meteor.*, **30**, 985–1004, <https://doi.org/10.1175/1520-0450-30.7.985>.
- McFarquhar, G. M., and A. J. Heymsfield, 1996: Microphysical characteristics of three anvils sampled during the Central Equatorial Pacific Experiment. *J. Atmos. Sci.*, **53**, 2401–2423, [https://doi.org/10.1175/1520-0469\(1996\)053,2401:MCOTAS.2.0.CO;2](https://doi.org/10.1175/1520-0469(1996)053,2401:MCOTAS.2.0.CO;2).
- , and —, 1997: Parameterization of tropical cirrus ice crystal size distributions and implications for radiative transfer: Results from CEPEX. *J. Atmos. Sci.*, **54**, 2187–2200, [https://doi.org/10.1175/1520-0469\(1997\)054<2187:POTCIC>2.0.CO;2](https://doi.org/10.1175/1520-0469(1997)054<2187:POTCIC>2.0.CO;2).
- , and —, 1998: The definition and significance of an effective radius for ice clouds. *J. Atmos. Sci.*, **55**, 2039–2052, [https://doi.org/10.1175/1520-0469\(1998\)055<2039:TDASOA>2.0.CO;2](https://doi.org/10.1175/1520-0469(1998)055<2039:TDASOA>2.0.CO;2).
- , and R. A. Black, 2004: Observations of particle size and phase in tropical cyclones: Implications for mesoscale modeling of microphysical processes. *J. Atmos. Sci.*, **61**, 422–439, [https://doi.org/10.1175/1520-0469\(2004\)061,0422:OOPSAP.2.0.CO;2](https://doi.org/10.1175/1520-0469(2004)061,0422:OOPSAP.2.0.CO;2).
- , H. Zhang, G. Heymsfield, R. Hood, J. Dudhia, J. B. Halverson, and F. Marks, 2006: Factors affecting the evolution of Hurricane Erin (2001) and the distributions of hydrometeors: Role of microphysical processes. *J. Atmos. Sci.*, **63**, 127–150, <https://doi.org/10.1175/JAS3590.1>.
- , M. S. Timlin, R. M. Rauber, B. F. Jewett, J. A. Grim, and D. P. Jorgensen, 2007: Vertical variability of cloud hydrometeors in the stratiform region of mesoscale convective systems and bow echoes. *Mon. Wea. Rev.*, **135**, 3405–3428, <https://doi.org/10.1175/MWR3444.1>.
- , B. F. Jewett, M. S. Gilmore, S. W. Nesbitt, and T. Hsieh, 2012: Vertical velocity and microphysical distributions related to rapid intensification in a simulation of Hurricane Dennis (2005). *J. Atmos. Sci.*, **69**, 3515–3534, <https://doi.org/10.1175/JAS-D-12-016.1>.
- , T. L. Hsieh, M. Freer, J. Mascio, and B. F. Jewett, 2015: The characterization of ice hydrometeor gamma size distributions as volumes in $N_0 - \lambda - \mu$ -phase space: Implications for microphysical process modeling. *J. Atmos. Sci.*, **72**, 892–909, <https://doi.org/10.1175/JAS-D-14-0011.1>.
- , and Coauthors, 2017: Processing of ice cloud in situ data collected by bulk water, scattering, and imaging probes: Fundamentals, uncertainties, and efforts toward consistency. *Ice Formation and Evolution in Clouds and Precipitation: Measurement and Modeling Challenges*, Meteor. Monogr., No. 58, Amer. Meteor. Soc., <https://doi.org/10.1175/AMSMONOGRAPH-D-16-0007.1>.
- Meyers, M. P., R. L. Walko, J. Y. Harrington, and W. R. Cotton, 1997: New RAMS cloud microphysics. Part II: The two-moment scheme. *Atmos. Res.*, **45**, 3–39, [https://doi.org/10.1016/S0169-8095\(97\)00018-5](https://doi.org/10.1016/S0169-8095(97)00018-5).
- Milbrandt, J. A., and M. K. Yau, 2005: A multimoment bulk microphysics parameterization. Part I: Analysis of the role of the spectral shape parameter. *J. Atmos. Sci.*, **62**, 3051–3064, <https://doi.org/10.1175/JAS3534.1>.
- Mitchell, D. L., 1996: Use of mass-and area-dimensional power laws for determining precipitation particle terminal velocities. *J. Atmos. Sci.*, **53**, 1710–1723, [https://doi.org/10.1175/1520-0469\(1996\)053<1710:UOMAAD>2.0.CO;2](https://doi.org/10.1175/1520-0469(1996)053<1710:UOMAAD>2.0.CO;2).
- , 2002: Effective diameter in radiation transfer: General definition, applications and limitations. *J. Atmos. Sci.*, **59**, 2330–2346, [https://doi.org/10.1175/1520-0469\(2002\)059<2330:EDIRTG>2.0.CO;2](https://doi.org/10.1175/1520-0469(2002)059<2330:EDIRTG>2.0.CO;2).
- , and W. P. Arnott, 1994: A model predicting the evolution of ice particle size spectra and radiative properties of cirrus clouds. Part II: Dependence of absorption and extinction on ice crystal morphology. *J. Atmos. Sci.*, **51**, 817–832, [https://doi.org/10.1175/1520-0469\(1994\)051<0817:AMPTEO>2.0.CO;2](https://doi.org/10.1175/1520-0469(1994)051<0817:AMPTEO>2.0.CO;2).
- , P. Rasch, D. Ivanova, G. McFarquhar, and T. Nousaininen, 2008: Impact of small ice crystal assumptions on ice sedimentation rates in cirrus clouds and GCM simulations. *Geophys. Res. Lett.*, **35**, L09806, <https://doi.org/10.1029/2008GL033552>.
- Moisseev, D. N., and V. Chandrasekar, 2007: Examination of the $\mu - \Lambda$ relation suggested for drop size distribution parameters. *J. Atmos. Oceanic Technol.*, **24**, 847–855, <https://doi.org/10.1175/JTECH2010.1>.
- Morrison, H., and W. Grabowski, 2008: A novel approach for representing ice microphysics in models: Description and tests using a kinematic framework. *J. Atmos. Sci.*, **65**, 1528–1548, <https://doi.org/10.1175/2007JAS2491.1>.
- , and J. A. Milbrandt, 2015: Parameterization of cloud microphysics based on the predictions of bulk ice particle properties. Part I: Scheme description and idealized tests. *J. Atmos. Sci.*, **72**, 287–311, <https://doi.org/10.1175/JAS-D-14-0065.1>.
- , G. Thompson, and V. Tatarkii, 2009: Impact of cloud microphysics on the development of trailing stratiform precipitation in a simulated squall line: Comparison of one- and two-moment schemes. *Mon. Wea. Rev.*, **137**, 991–1007, <https://doi.org/10.1175/2008MWR2556.1>.
- , J. A. Milbrandt, G. H. Bryan, K. Ikeda, S. A. Tessendorf, and G. Thompson, 2015: Parameterization of cloud microphysics based on the prediction of bulk ice particle properties. Part II: Case study comparisons with observations and other schemes. *J. Atmos. Sci.*, **72**, 312–339, <https://doi.org/10.1175/JAS-D-14-0066.1>.
- Moshtagh, N., 2006: Minimum volume enclosing ellipsoids. MATLAB, accessed 20 December 2019, <https://www.mathworks.com/matlabcentral/fileexchange/9542-minimum-volume-enclosing-ellipsoid>.
- Murphy, A. M., R. M. Rauber, G. M. McFarquhar, J. A. Finlon, D. M. Plummer, A. A. Rosenow, and B. F. Jewett, 2017: A microphysical analysis of elevated convection in the comma head region of continental winter cyclones. *J. Atmos. Sci.*, **74**, 69–91, <https://doi.org/10.1175/JAS-D-16-0204.1>.
- Protat, A., and Coauthors, 2016: The measured relationship between ice water content and cloud radar reflectivity in tropical convective clouds. *J. Appl. Meteor. Climatol.*, **55**, 1707–1729, <https://doi.org/10.1175/JAMC-D-15-0248.1>.
- Qu, Z., and Coauthors, 2018: Evaluation of a high-resolution numerical weather prediction model's simulated clouds using observations from CloudSat, GOES-13 and in situ aircraft. *Quart. J. Roy. Meteor. Soc.*, **144**, 1681–1694, <https://doi.org/10.1002/qj.3318>.
- Ratavsky, T. P., and Coauthors, 2019: Summary of the High Ice Water Content (HIWC) RADAR flight campaigns. SAE Tech. Paper 2019-01-2025, NASA/TM-2020-220306, <https://doi.org/10.4271/2019-01-2027>.
- Sanderson, B. M., C. Piani, W. J. Ingram, D. A. Stone, and M. R. Allen, 2008: Towards constraining climate sensitivity by linear analysis of feedback patterns in thousands of perturbed-physics

- GCM simulations. *Climate Dyn.*, **30**, 175–190, <https://doi.org/10.1007/s00382-007-0280-7>.
- Schlüsse, I., A. Macke, and J. Reichardt, 2005: The impact of ice crystal shapes, size distributions, and spatial structures of cirrus clouds on solar radiative fluxes. *J. Atmos. Sci.*, **62**, 2274–2283, <https://doi.org/10.1175/JAS3459.1>.
- Seifert, A., and K. Beheng, 2006: A two-moment cloud microphysics parameterization for mixed-phase clouds. Part 1: Model description. *Meteor. Atmos. Phys.*, **92**, 45–66, <https://doi.org/10.1007/s00703-005-0124-4>.
- Smith, P. L., 1984: Equivalent radar reflectivity factors for snow and ice particles. *J. Climate Appl. Meteor.*, **23**, 1258–1260, [https://doi.org/10.1175/1520-0450\(1984\)023<1258:ERRFFS>2.0.CO;2](https://doi.org/10.1175/1520-0450(1984)023<1258:ERRFFS>2.0.CO;2).
- , —, and D. V. Kliche, 2005: The bias in moment estimators for parameters of drop size distribution functions: Sampling from exponential distributions. *J. Appl. Meteor.*, **44**, 1195–1205, <https://doi.org/10.1175/JAM2258.1>.
- , —, and R. W. Johnson, 2009: The bias and error in moment estimators for parameters of drop size distribution functions: Sampling from gamma distributions. *J. Appl. Meteor. Climatol.*, **48**, 2118–2126, <https://doi.org/10.1175/2009JAMC2114.1>.
- SPEC, 2011: 2D-S Post-processing using 2D-S View Software: User manual, version 1.1. SPEC Inc., 48 pp.
- Stanford, M. W., H. Morrison, A. Varble, J. Berner, W. Wu, G. McFarquhar, and J. Milbrandt, 2019: Sensitivity of simulated deep convection to a stochastic ice microphysics framework. *J. Adv. Model. Earth Syst.*, **11**, 3362–3389, <https://doi.org/10.1029/2019MS001730>.
- Stephens, G. L., 2005: Cloud feedbacks in the climate system: A critical review. *J. Climate*, **18**, 237–273, <https://doi.org/10.1175/JCLI-3243.1>.
- Straka, J. M., and E. R. Mansell, 2005: A bulk microphysics parameterization with multiple ice precipitation categories. *J. Appl. Meteor.*, **44**, 445–466, <https://doi.org/10.1175/JAM2211.1>.
- Strapp, J. W., and Coauthors, 2016a: The high ice water content (HIWC) study of deep convective clouds: Science and technical plan. FAA Rep., DOT/FAA/TC-14/31, 105 pp.
- , L. E. Lillie, T. P. Ratovsky, C. R. Davison, and C. Dumont, 2016b: Isokinetic TWC evaporator probe: Development of the IKP2 and performance testing for the HAIC-HIWC Darwin 2014 and Cayenne Field Campaigns. *Proc. Eighth AIAA Atmospheric and Space Environments Conf.*, AIAA-2016-4059, Washington, DC, American Institute of Aeronautics and Astronautics, <http://arc.aiaa.org/doi/10.2514/6.2016-4059>.
- , —, and Coauthors, 2020: An assessment of cloud total water content and particle size from light test campaign measurements in high ice water content, mixed phase/ice crystal icing conditions: Primary in-situ measurements. FAA Rep., AU5 DOT/FAA/TC-18/1, 262 pp.
- , —, and Coauthors, 2021: Comparisons of cloud in situ microphysical properties of deep convective clouds to appendix D/P using data from the high-altitude ice crystals-high ice water content and high ice water content-RADAR I flight campaigns. *SAE Int. J. Aerosp.*, **14**, 127–159, <https://doi.org/10.4271/01-14-02-0007>.
- Thompson, G., P. R. Field, R. M. Rasmussen, and W. D. Hall, 2008: Explicit forecasts of winter precipitation using an improved bulk microphysics scheme. Part II: Implementation of a new snow parameterization. *Mon. Wea. Rev.*, **136**, 5095–5115, <https://doi.org/10.1175/2008MWR2387.1>.
- Tian, L., G. M. Heymsfield, L. Li, A. J. Heymsfield, A. Bansemir, C. H. Twohy, and R. C. Srivastava, 2010: A study of cirrus ice particle size distribution using TC4 observations. *J. Atmos. Sci.*, **67**, 195–216, <https://doi.org/10.1175/2009JAS3114.1>.
- Van Weverberg, K., N. P. M. van Lipzig, and L. Delobbe, 2011: The impact of size distribution assumptions in a bulk one-moment microphysics scheme on simulated surface precipitation and storm dynamics during a low-topped supercell case in Belgium. *Mon. Wea. Rev.*, **139**, 1131–1147, <https://doi.org/10.1175/2010MWR3481.1>.
- Varley, D. J., 1978: Cirrus particle distribution study, Part I. Air Force Geophysical Laboratory Rep. AFGL-TR-78-0192, 71 pp.
- Waitz, F., M. Schnaiter, T. Leisner, and E. Järvinen, 2021: PHIPS-HALO: The airborne Particle Habit Imaging and Polar Scattering probe—Part 3: Single-particle phase discrimination and particle size distribution based on the angular-scattering function. *Atmos. Meas. Tech.*, **14**, 3049–3070, <https://doi.org/10.5194/amt-14-3049-2021>.
- Walko, R. L., W. R. Cotton, M. P. Meyers, and J. Y. Harrington, 1995: New RAMS cloud microphysics. Part I: The one-moment scheme. *Atmos. Res.*, **38**, 29–62, [https://doi.org/10.1016/0169-8095\(94\)00087-T](https://doi.org/10.1016/0169-8095(94)00087-T).
- Wang, Y., 2002: An explicit simulation of tropical cyclones with a triply nested movable mesh primitive equation model: TCM3. Part II: Model refinements and sensitivity to cloud microphysics parameterization. *Mon. Wea. Rev.*, **130**, 3022–3036, [https://doi.org/10.1175/1520-0493\(2002\)130<3022:AESOTC>2.0.CO;2](https://doi.org/10.1175/1520-0493(2002)130<3022:AESOTC>2.0.CO;2).
- Welch, R. M., S. K. Cox, and J. M. Davis, 1980: *Solar Radiation and Clouds*. Meteor. Monogr., No. 39, Amer. Meteor. Soc., 93 pp.
- Wolde, M., C. Nguyen, A. Korolev, and M. Bastian, 2016: Characterization of the Pilot X-band radar responses to the HIWC environment during the Cayenne HAIC-HIWC 2015 campaign. *Eighth AIAA Atmospheric and Space Environments Conf.*, AIAA 2016-4201, Washington, DC, American Institute of Aeronautics and Astronautics, <https://doi.org/10.2514/6.2016-4201>.
- Wolf, V., T. Kuhn, and M. Krämer, 2019: On the dependence of cirrus parametrizations on the cloud origin. *Geophys. Res. Lett.*, **46**, 12565–12571, <https://doi.org/10.1029/2019GL083841>.
- Wong, R. K. W., and N. Chidambaram, 1985: Gamma size distribution and stochastic sampling errors. *J. Climate Appl. Meteor.*, **24**, 568–579, [https://doi.org/10.1175/1520-0450\(1985\)024<0568:GSDASS>2.0.CO;2](https://doi.org/10.1175/1520-0450(1985)024<0568:GSDASS>2.0.CO;2).
- , —, L. Cheng, and M. English, 1988: The sampling variations of hailstone size distributions. *J. Appl. Meteor.*, **27**, 254–260, [https://doi.org/10.1175/1520-0450\(1988\)027<0254:TSVOHS>2.0.CO;2](https://doi.org/10.1175/1520-0450(1988)027<0254:TSVOHS>2.0.CO;2).
- Wu, W., and G. M. McFarquhar, 2016: On the impacts of different definitions of maximum dimension for nonspherical particles recorded by 2D imaging probes. *J. Atmos. Oceanic Technol.*, **33**, 1057–1072, <https://doi.org/10.1175/JTECH-D-15-0177.1>.
- Wylie, D., D. L. Jackson, W. P. Menzel, and J. J. Bates, 2005: Trends in global cloud cover in two decades of HIRS observations. *J. Climate*, **18**, 3021–3031, <https://doi.org/10.1175/JCLI3461.1>.
- Yost, C. R., and Coauthors, 2018: A prototype method for diagnosing high ice water content probability using satellite imager data. *Atmos. Meas. Tech.*, **11**, 1615–1637, <https://doi.org/10.5194/amt-11-1615-2018>.

- Zender, C. S., and J. T. Kiehl, 1997: Sensitivity of climate simulations to radiative effects of tropical anvil structure. *J. Geophys. Res.*, **102**, 23 793–23 803, <https://doi.org/10.1029/97JD02009>.
- Zhao, Y., G. G. Mace, and J. M. Comstock, 2010: The occurrence of particle size distribution bimodality in midlatitude cirrus from ground-based remote sensing data. *J. Atmos. Sci.*, **68**, 1162–1167, <https://doi.org/10.1175/2010JAS3354.1>.
- Zhu, T., and D. Zhang, 2006: Numerical simulation of Hurricane Bonnie (1998). Part II: Sensitivity to varying cloud microphysical processes. *J. Atmos. Sci.*, **63**, 109–126, <https://doi.org/10.1175/JAS3599.1>.
- Zipser, E. J., C. Liu, D. J. Cecil, S. W. Nesbitt, and D. P. Yorty, 2006: Where are the most intense thunderstorms on Earth? *Bull. Amer. Meteor. Soc.*, **87**, 1057–1071, <https://doi.org/10.1175/BAMS-87-8-1057>.